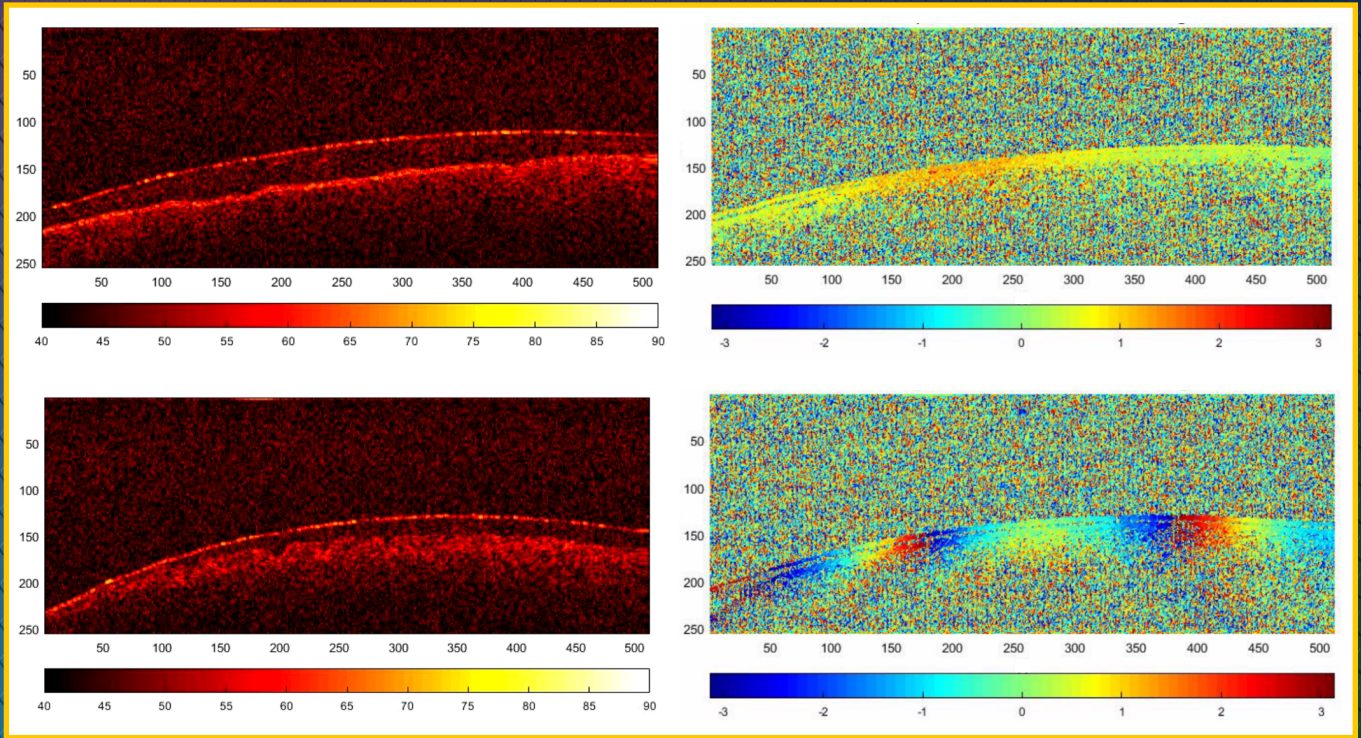
Volume 8, Issue 2, 2022

Journal of Biomedical Photonics & Engineering

Special Issue

"Laser and optical technologies in biomedicine and ecology"



Special issue Editors:
Ivan A. Bratchenko and Aleksandra M. Mayorova

© 2022 J-BPE

Journal of Biomedical Photonics & Engineering

by Samara National Research University

Volume 8, Issue 2 (June 2022)

Special Issue
"Laser and optical technologies in biomedicine and ecology"

Special Issue Editors

Ivan A. Bratchenko
Samara National Research University, Russia

Aleksandra M. Mayorova
Samara Branch of P.N. Lebedev Physical Institute of Russian Academy of Sciences, Russia

Editor-In-Chief

Valery V. Tuchin - Saratov National Research State University, Russian Federation;
Institute of Precision Mechanics and Control RAS, Russian Federation; a corr.-member of RAS

Deputy Editor-In-Chief

Valery P. Zakharov - Samara National Research University, Russian Federation

Postal address:
39B Lukacheva st., room #301
Samara 443086, Russian Federation

Used Figure from this issue on the Cover

Olga I. Baum et al., *Laser Effect on a Pathologically Altered Capsule of the Lens of the Eye*, 020302, Figs. 6 and 7 (*adapted*).

© 2022 J-BPE

Contents

Introduction

Foreword to the Special Issue on Laser and optical technologies in biomedicine and ecology 020101

Articles

The Reaction of the Methylidyne Radical (CH X2Π) with the Hydrogen Cyanide (HCN X1∑+) Molecule in Cold Molecular Clouds and Planetary Atmospheres 020301
Lubov I. Krikunova, Anatoliy A. Nikolayev, Denis P. Porfirev, and Alexander M. Mebel

Laser Effect on a Pathologically Altered Capsule of the Lens of the Eye 020302
Olga I. Baum, Ekaterina M. Kasianenko, Alexey V. Yuzhakov, Alibek A. Gamidov, Elena P. Medvedeva, and Yusef N. Yusef

Optical Properties of Glycated and Non-Glycated Hemoglobin – Raman/Fluorescence Spectroscopy and Refractometry 020303
Ekaterina N. Lazareva, Andrey Y. Zyubin, Natalya I. Dikht, Alla B. Bucharskaya, Ilya G. Samusev, Vasily A. Slezhkin, Vyacheslav I. Kochubey, and Valery V. Tuchin

Porous Silicon Nanoparticles with Rare Earth as Potential Contrast Agents for MRI and Luminescent Probes for Bioimaging 020304
Anastasiya D. Mironova, Yulia V. Kargina, Olga S. Pavlova, Alexander M. Perepukhov, Igor O. Sobina, and Victor Yu. Timoshenko

Study of Laser-Induced Microdeformations of the Cornea Using Phase-Sensitive Optical Coherent Elastography 020305
Ekaterina M. Kasianenko, Anastasia V. Golovchenko, Vladimir I. Siplivyi, Oleg G. Romanov, and Olga I. Baum

Investigation of Porous Silicon Nanocomposites with Hydroxyapatite Powder Solubility 020306
Andrey N. Agafonov, Diana Suyundukova, Natalya V. Latukhina, and Alexander V. Pavlikov

 © 2022 J-BPE

 doi: 10.18287/JBPE21.08.020101

Foreword to the Special Issue on Laser and optical technologies in biomedicine and ecology

Dear Colleagues,

We are glad to present you the Special Issue of the Journal of Biomedical Photonics & Engineering (J-BPE) with selected papers of the Biophotonics Workshop of the XIX All-Russian Youth Conference-Contest on Optics and Laser Physics (Samara, November 9-12, 2021). The conference-contest was organized by P.N. Lebedev Physical Institute (Samara Branch) and Samara National Research University and supported by Administration of Samara Region and Samara SPIE Student Chapter.

The program of the Biophotonics Workshop 2021 included lectures by leading scientists, invited reports as well as competitive oral and poster reports of young scientists from Samara, Moscow, Nizhny Novgorod, Saratov, Orel, and Astrakhan.

The lectures and invited reports aroused great interest. For example, in his lecture "*Light as a factor in plant development control*", **Academician** of the RAS **Yu. N. Kulchin** (Institute of Automation and Control Processes FEB of RAS, Vladivostok) spoke about the study on the effect of a change in the spectral composition and intensity of polychromatic radiation on the development of plants and their production of primary and secondary metabolites. **Dr. A. A. Fronya** presented topical results of research on the effect of ultraviolet radiation in the UVA wavelength range on the infectious properties of coronavirus conducted by the Lebedev Physical Institute together with the Gamaleya National Research Center.

The materials of the invited report of **Ekaterina M. Kasianenko** (Institute of Photonic Technologies Federal State Institution "Research Center "Crystallography and Photonics" RAS) *"Laser action on a pathologically altered capsule of the lens of the eye"* and coauthors are presented in the Special Issue of J-BPE. In the paper **Olga I. Baum** et al., the biomechanics of the lens - capsular bag system and the influence of various parameters of laser exposure on it were studied.

In the paper **Ekaterina M. Kasianenko** et al., the possibilities of phase-sensitive optical coherent elastography to register laser-induced microdeformations of the cornea under various mechanical stresses are demonstrated.

Anastasiya D. Mironova (Phys-Bio Institute, National Research Nuclear University "MEPhI", Moscow, Russia) et al. demonstrated the capability to use mesoporous silicon nanoparticles (MSP NPs) doped with gadolinium as contrast agents for MRI, and MSP NPs doped with europium as luminescent probes for bioimaging. The results were obtained on the base of measurements of proton relaxation in aqueous suspensions of nanoparticles with embedded ions of rare earth and study of the photoluminescence spectra of the samples.

 doi: 10.18287/JBPE21.08.020101

Note, that Anastasia became the winner of the Biophotonics section in the Oral Presentations nomination.

The international group of authors (Samara branch of Lebedev Physical Institute, Samara University and Florida International University) in the publication by **Lubov Krikunova** et al. studied the reaction of the methylidyne radical with the hydrogen cyanide molecule in cold molecular clouds and Planetary Atmospheres. The reaction under study can be considered as the first stage of chemical evolution, as a result of which organic compounds are formed from the simplest molecules. These organic compositions can generate polycyclic organic compounds, which can be considered as an initial stage of abiogenesis leading to the synthesis of the most basic amino acids.

Ekaterina N. Lazareva (Saratov State University and Tomsk State University) compares the optical properties of glycated (HbA1c) and non-glycated (Hb) hemoglobin using Surface-enhanced Raman spectroscopy (SERS), spectrofluorimetry, and refractometry. Good discrimination between two hemoglobins indicating differences in their molecular structure was demonstrated by means of SERS and fluorescence spectra. Also, for the first time refractive index temperature increments were measured for HbA1c in a wide wavelength range in the visible and NIR.

Agafonov et al. from Samara University in their article proposed to use the porous silicon-hydroxyapatite system as an effective matrix for creating nanocomposites for osteoplasty. They studied the change in the structure of the aqueous suspension of the porous silicon+hydroxyapatite nanocomposite powder over time to assess the possibility of its dissolution in physiological fluids.

Thus, the articles collected in this special issue highlight the potential of optical and laser technologies in modern medical, biological and environmental applications, and even touch upon the origin of organic compounds in the Universe.

We invite everyone to take part in the XX All-Russian competition-conference in optics and laser physics, dedicated to the 100th anniversary of the birth of N. G. Basov, which will be held in Samara on November 8-12, 2022.

Special Issue Editors:

Ivan A. Bratchenko

Samara National Research University

E-mail: iabratchenko@gmail.com

Aleksandra M. Mayorova

Samara Branch of P.N. Lebedev Physical Institute of Russian Academy of Sciences

E-mail: mayorovaal@gmail.com

The Reaction of the Methylidyne Radical (CH $X^2\Pi$) with the Hydrogen Cyanide (HCN $X^1\sum^+$) Molecule in Cold Molecular Clouds and Planetary Atmospheres

Lubov I. Krikunova[1,2*], Anatoliy A. Nikolayev[1,2], Denis P. Porfirev[1,2], and Alexander M. Mebel[3]

[1] Lebedev Physical Institute, 221 Novo-Sadovaya str., Samara 443011, Russia

[2] Samara National Research University, 34 Moskovskoe shosse, Samara 443086, Russia

[3] Department of Chemistry and Biochemistry, Florida International University, 11200 SW 8th str., Miami, Florida 33199, USA

*** e-mail:** lubov13markova@gmail.com

Abstract. The reaction of the methylidyne (CH; $X^2\Pi$) radical with hydrogen cyanide (HCN; $X_1\sum$) molecule was studied at a collision energy of 4.0 kJ/mol with ab initio calculations of the potential energy surface (PES). Geometries and potential energies of reactants, products, intermediates and transition states (TS) for the reaction were found by means of ab initio quantum chemical method ωB97xd/cc-pVTZ and the higher-level corrections were evaluated at the CCSD(T)-F12 level of theory with the cc-pVQZ-f12 (E_1) and cc-pVTZ-f12 (E_2) basis sets. The calculated values then were used for extrapolation to the complete basis set (CBS) limit using the two-point expression $E(CBS) = E_1 + 0.69377 \times (E_1 - E_2)$. Analysis of the found energies, structural and kinetic characteristics of the involved compounds allowed us to determine the reaction paths leading to the formation of linear and cyclic intermediates, as well as to the formation of atomic and molecular hydrogen. Those results were utilized in Rice−Ramsperger−Kassel−Marcus calculations of the product branching ratios at the zero pressure limit – common approach in modelling of the cold molecular clouds chemistry. Mechanism identified emphasizes importance of the CH+HCN reaction as an important supplier of the initial bricks for building heterocyclic hydrocarbons in extreme environments.
© 2022 Journal of Biomedical Photonics & Engineering.

Keywords: potential energy surface; rate constants; density functional theory; methylidyne; hydrogen cyanide; cyanomethylidyne; cyanomethylene.

Paper #3476 received 19 Feb 2022; revised manuscript received 03 Apr 2022; accepted for publication 03 Apr 2022; published online 28 Apr 2022. doi: 10.18287/JBPE22.08.020301.

1 Introduction

A wide variety of chemical elements and even complex molecular compounds, including organic ones, were found in space using spectroscopy methods [1]. Carbon, nitrogen, and hydrogen atoms are common constituents of interstellar clouds and planetary atmospheres. Among the complex molecules there are “prebiotic” compounds, such as aminoacetonitrile, which can participate in the formation of glycine, the simplest amino acid. Ribose, the basis of organic life, can also be formed in molecular clouds [2]. If such compounds fall into favorable conditions, this will already be precursors for the emergence of life.

The methylidyne radical (CH, $X^2\Pi$) represents the simplest organic radical, highly reactive and able to interact with neutral molecules [3]. It plays an important role in various chemical environments ranging from the hydrocarbon combustion, dense interstellar clouds, and in planetary atmospheres. Since the very first detection of the methylidyne radical in the interstellar medium in 1937, methylidyne has been dubbed “ubiquitous” in deep space and has been observed toward diffuse clouds namely ζ Per [4], molecular clouds like TMC-1 [5, 6],

and star forming regions such as SgrB2 [7–10]. Reactions involving the CH radical provide one of the ways to synthesize long hydrocarbons and complex organic molecules in dense interstellar clouds and planetary atmospheres [11].

Methylidyne is the result of the photodissociation of methane in the Lyman series Ly-α line. Methane is known to be present in appreciable amounts in interstellar clouds. The decay of methane, either by absorbing photons or colliding with energetic particles, begins a complex chemical evolution that can form cyclic and linear organic molecules. The fact that low-temperature experimental rate constants for various reactions of CH with organic molecules are typically on the order of 10^{-10} cm^3 mol^{-1} s^{-1} suggests that the CH radical is indeed sufficiently reactive for its reactions with the hydrogen cyanide molecule to be significant both in cold molecular clouds, and in the planetary atmospheres [12]. Thus, the experimental temperature dependence of the total rate constants of the reactions of methylidyne with unsaturated organic molecules suggests that these reactions proceed without any barriers. Since the CH radical has a high enthalpy of formation, 596.40 kJ/mol, there are many thermodynamically accessible channels for the reactions of the methylidyne radical with unsaturated organic molecules. The identification of products and the determination of their branching factors are particularly important for obtaining reliable simulations of complex chemistry such as interstellar chemistry [11].

2 Computational methods

The long-range corrected hybrid density functional ωB97xd [13, 14] with the cc-pvtz [15] basis set was used for geometry optimization of different species on the C_2H_2N potential energy surface (PES) accessed by the methylidyne plus hydrogen cyanide molecule reaction, including the reactants, products, intermediates, and transition states (TS). The same ωB97xd/cc-pvtz level of theory was then employed to compute vibrational frequencies for each stationary structure. The frequencies were utilized in the evaluation of zero-point vibrational energy corrections (ZPE) and in the calculations of rate constants. In order to obtain chemically accurate relative energies of various species on the C_2H_2N PES, the explicitly correlated couple clusters method with single and double excitations and with perturbative treatment of triple excitations CCSD(T)-F12 [16, 17] in conjunction with Dunning's correlation-consistent cc-pVTZ-f12 and cc-pVQZ-f12 basis sets was used to refine single-point energies of all optimized structures. The final energies of all structures were extrapolated to the complete basis set (CBS) [18] limit using the two-point expression:

$$E(CSB) = E_1 + 0.69377 \times (E_1 - E_2), \quad (1)$$

where

$$E_1 = E(CCSD(T) - F12 / cc - pVTZ - f12),$$
$$E_2 = E(CCSD(T) - F12 / cc - pVQZ - f12). \quad (2)$$

Relative energies are anticipated to be accurate within 1 kcal/mol or even better [19]. The GAUSSIAN 09 [20] and MOLPRO 2010 [21] quantum chemistry software codes were used for the *ab initio* calculations.

The Rice−Ramsperger−Kassel−Marcus (RRKM) approach utilizing the energetic and molecular parameters from the electronic structure calculations was employed to evaluate energy-dependent rate constants for all unimolecular reaction steps taking place on the C_2H_2N PES following the initial bimolecular association stage [22]. In the calculations of the energy-dependent rate constants, the internal energy for each C_2H_2N intermediate or transition state was assumed to be equal to the sum of the collision and chemical activation energies, where the chemical activation energy is a negative of the relative energy of the species relative to the separated methylidyne plus hydrogen cyanide reactants. Rate constants were evaluated as functions of the available internal energy of each intermediate or transition state within the harmonic approximation using ωB97xd/cc-pVTZ frequencies and employing our in-house code Unimol [23, 24]. Unimol is an updated version of our previous software code on energy dependent RRKM calculations of rate constants for multiwell and multichannel unimolecular reactions under single-collision conditions and for solving a system of first-order kinetic equations. Unimol automatically processes GAUSSIAN 09 log files to compute numbers of states for transition states and densities of states for local minima employing the direct count method. The internal energy is assumed to be equal to the sum of the collision energy and the chemical activation energy, that is, negative of the relative energy of a species with respect to the reactants. Only one energy level is considered throughout as at a zero-pressure limit corresponding to crossed molecular beams conditions. RRKM rate constants are then used to compute product branching ratios by solving first-order kinetic equations within steady-state approximation.

3 Results & Discussion

3.1 Initial adducts

Initial adducts are listed in Fig. 1.

The barrierless reactions are initiated through addition of the methylidyne radical to the nitrogen atom of the hydrogen cyanide molecule with the intermediate w1 (–41.8 kcal/mol) formation. An alternative way is methylidyne radical addition to the carbon atom of the hydrogen cyanide molecule with the intermediate w2 (– 53 kcal/mol) formation. As a result of the methylidyne radical addition to the triple C–N bond of the hydrogen cyanide molecule the cyclic intermediate w3 is formed

(–50.4 kcal/mol). The intermediate w4 (–104.5 kcal/mol) can be formed if the methylidyne radical inserts into the C–H bond of the hydrogen cyanide molecule.

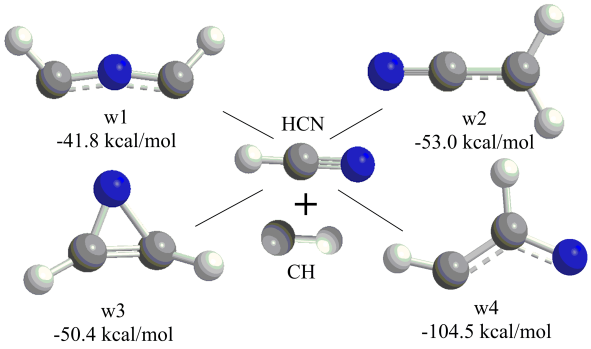


Fig. 1 Initial adducts in the barrierless reaction.

Studied reactions of the methylidyne radical with organic molecules demonstrate that a ratio in the entrance channels of multiple bond addition and C–H bond insertion of about 85:15, which can be understood in terms of a reduced cone of acceptance of the C–H σ-bond compared to the π electrons of the multiple bond [25]. There are the similar reaction dynamics mechanisms in the CH+HCN reaction, suggesting that methylidyne radical addition to the carbon or nitrogen atom or C–N triple bond of HCN is likely the dominant entrance channel [12].

3.2 Potential energy surface

Simplified complete PES diagram (Fig. 2) demonstrates the most energetically favorable reaction paths. Detailed molecular structures are presented in Fig. 3. The PES could be partitioned into two branches leading towards linear or cyclic structures. The first one mostly stems from w4 (–104.5 kcal/mol) intermediate and its predecessor w2 (–53.0 kcal/mol), which are connected through transition state b2 with relative to reagents energy of –9.9 kcal/mol. There are three possible paths from w4. The first two ones are direct hydrogen atom/molecule losses. Elimination of H-atom is barrierless and results in formation of cyanomethylene (product p1: –0.6 kcal/mol). Hydrogen molecule separation requires to overcome b2 barrier, which relative energy is 3.6 kcal/mol less than that of p1, and leads to cyanomethylidyne (product p2: –12.2 kcal/mol). The third way includes additional step – bend of the CCN chain w4 → b6 → w6, with barrier of –52.8 kcal/mol in forward and –2.1 kcal/mol in backward directions. Then the nitrogen atom could be inserted between carbon atoms through low energy barrier b8: only –1.1 kcal/mol to form w9 (–81.1 kcal/mol) and –28.6 kcal/mol to activate reverse transformation. The second branch of the PES starts in w1 (–41.8 kcal/mol) which precedes cyclic intermediate w3 (–50.4 kcal/mol). That triangular structure could be transformed into aforementioned w9 by shifting of H-atom from one carbon to another and simultaneous cleavage of CC-bond, which possesses moderate for the PES barrier b5 of –41.9 kcal/mol in w3 → w9 direction and relatively high one of –72.6 kcal/mol for the reverse step. Path to another cyclic molecule w7 (–25.9 kcal/mol) branches off after hydrogen jump from one of the carbon atoms to nitrogen w3 → b3 → w5. Barrier for that isomerization is of 33.5 kcal/mol, which is more than 4 times higher than for the reverse step (8.1 kcal/mol). Two paths lead to w7. The first one is immediate cycle reclosure w5 → b7 → w7 with low barrier of 6.1 kcal/mol to overcome. The second transformation includes additional NH-group shift w5 → b4 (–13.1 kcal/mol) → w8 (–72.6 kcal/mol) → b9 (–10.3 kcal/mol) → w7.

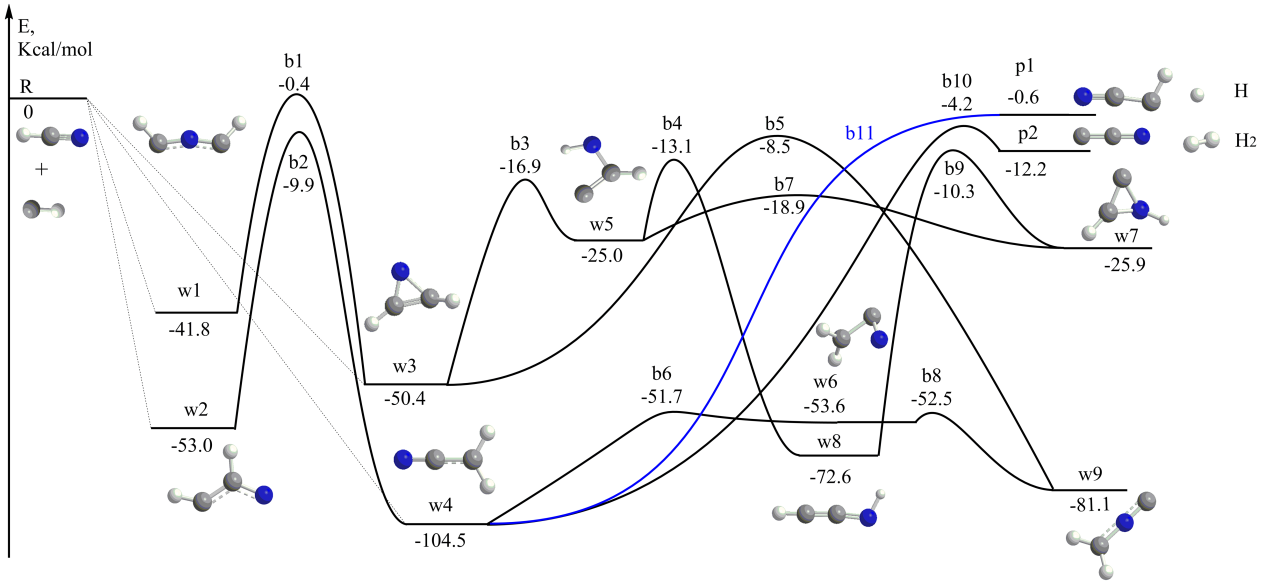


Fig. 2 The HCN+CH reaction potential energy surface.

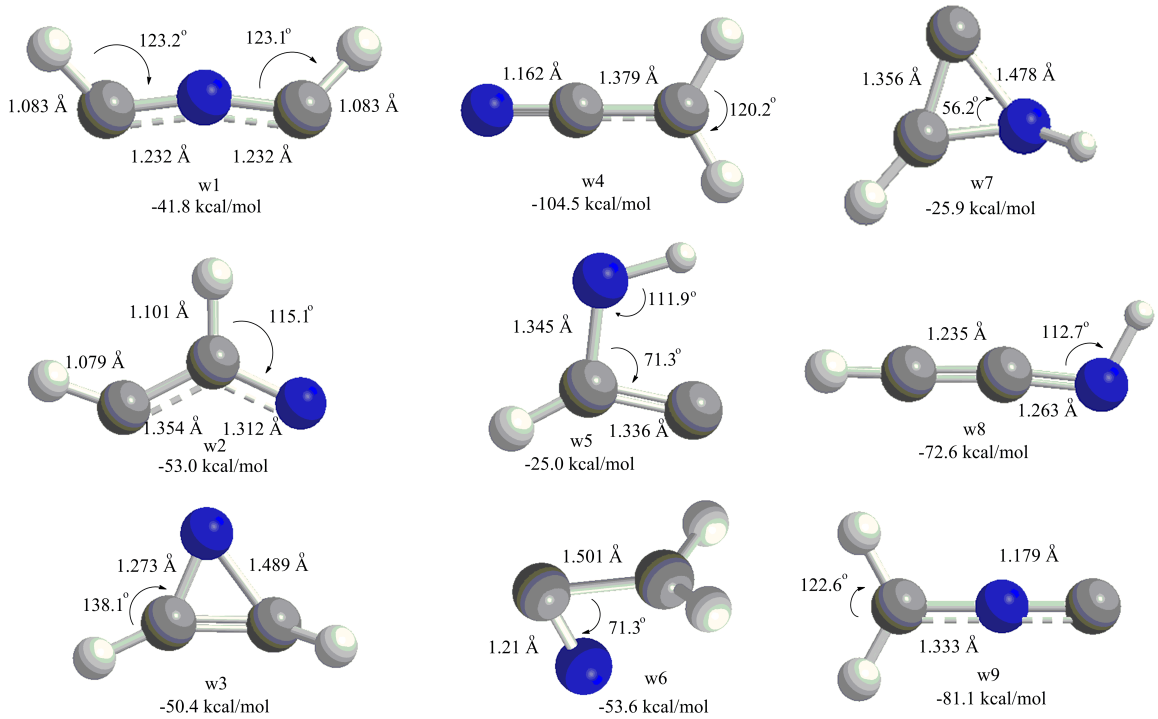


Fig. 3 Detailed molecular structures of intermediates of interest.

From the PES, we can infer that stabilization in the w8-well should not play an important role in the whole dynamics, because of energetically favorable direct step w5 → b7 → w7, which also possesses significantly lower barriers to proceed. Regarding products, entropically factors play in favor of cyanomethylene production, whereas it requires slightly more energy. Thus, the final answer about relative yields of those molecules could be given only after kinetic calculations.

3.3 Rate constants

Rate constants evaluated are listed in Table 1. As predicted, steps w8 → w5 and w8 → w7 are one of the slowest. However, stabilization still could make some impact, because the rate constants for w5 → w8 and w5 → w7 isomerizations are of the same order. The rate constant of p1-formation from w4 adduct is more than two times higher than one for p2.

Table 1 Rate constant.

Step	k, s^{-1}	Step	k, s^{-1}
w4→p1	5.08E+10	w3→w9	6.44E+10
w4→p2	2.37E+10	w9→w3	3.04E+09
w8→w7	2.35E+09	w5→w8	2.30E+12
w7→w8	1.89E+12	w8→w5	4.22E+09
w9→w6	9.73E+11	w3→w5	2.53E+11
w6→w9	3.26E+13	w5→w3	3.03E+12
w5→w7	3.95E+12	w2→w4	8.88E+09
w7→w5	5.82E+12	w4→w2	6.40E+09
w6→w4	2.65E+13	w1→w3	3.39E+09
w4→w6	7.61E+11	w3→w1	5.23E+09

Corresponding statistical yields were determined using RRKM theory. Since the initial adducts w1–w4 can rearrange to each other via barriers that are lower than dissociation barriers, the resulting product branching ratios from RRKM calculations appear to be practically independent of the initial intermediate. RRKM theory predicts the HCCN product (p1) along with atomic hydrogen to be the most likely product (~68.2%) followed by the CCN (p2) product along with molecular hydrogen (~31.8%).

4 Conclusion

The reaction of the unsaturated hydrogen cyanide molecule HCN with the methylidyne radical CH was studied. Because of the highly reactive nature of methylidyne, the reaction does not have entry barriers. Moreover, the relative energy of every intermediate, product and transition state on the presented PES is lower than that of reactants. Moreover, relative energy of every intermediate, product and transition state on the presented PES is lower than that of reagents. Which allows us to state, that proposed mechanism is feasible even in cold interstellar media. Simple one- or two-step paths leading towards the growth of linear molecules are revealed. Formation of the first one, cyanomethylene, significantly outstrips that of the runner-up, cyanomethylidyne, with relative yields ~68.2% and ~31.8% respectively. Investigated reaction could be treated as the first step of chemical evolution resulting in the formation of organic compounds from the simplest molecules. These organic species can in turn trigger reactions that generate polycyclic organic compounds, which can be considered as an initial stage of abiogenesis leading to the synthesis of the most basic amino acids.

Disclosures

All authors declare that there is no conflict of interests in this paper.

References

1. M. Ohishi, "Search for complex organic molecules in space," Journal of Physics: Conference Series 728(5), 052002 (2016).
2. M. Nuevo, E. Sciamma-O'Brien, S. A. Sandford, F. Salama, C. K. Materese, and A. L. D. Kilcoyne, "The Titan haze simulation (THS) experiment on COSmIC. part III. XANES study of laboratory analogs of titan tholins," Icarus 376, 114841 (2022).
3. C. Romanzin, "Methane photochemistry: A brief review in the frame of a new experimental program of Titan's atmosphere simulations," Advances in Space Research 36(2), 258–267 (2005).
4. H. Wiesemeyer, R. Güsten, K. M. Menten, C. A. Durán, T. Csengeri, A. M. Jacob, R. Simon, J. Stutzki, and F. Wyrowski, "Unveiling the chemistry of interstellar CH-Spectroscopy of the 2 THz N= 2←1 ground state line," Astronomy & Astrophysics 612, A37 (2018).
5. D. Xu, D. Li, "CH as a molecular gas tracer and c-shock tracer across a molecular cloud boundary in Taurus," The Astrophysical Journal 833(1), 90 (2016).
6. K. Sellgren, R. G. Smith, and T. Y. Brooke, "The 3.2 – 3.6 Micron Spectra of Monoceros R2/IRS-3 and Elias 16," Astrophysical Journal 433, 179–186 (1994).
7. B. Larsson, R. Liseau, "Gas and dust in the star-forming region ρ Oph A – II. The gas in the PDR and in the dense cores," Astronomy & Astrophysics 608, A133 (2017).
8. Y. C. Minh, H. B. Liu, and R. Galvan´-Madrid, "Chemical diagnostics of the massive star cluster-forming cloud G33.92+0.11. I. CS, CH3OH, CH3N, OCS, H2S, SO2, and SiO," Astrophysical Journal 824(2), 99 (2016).
9. O. Kochina, D. Wiebe, "Organic compounds in star forming regions," Origins of Life and Evolution of the Biospheres 44(3), 169–174 (2014).
10. J. L. Neill, E. A. Bergin, D. C. Lis, P. Schilke, N. R. Crockett, C. Favre, M. Emprechtinger, C. Comito, S.-L. Qin, D. E. Anderson, A. M. Burkhardt, C. Jo-Hsin, B. J. Harris, S. D. Lord, B. A. McGuire, T. D. McNeill, R. R. Monje, T. G. Phillips, A. L. Steber, T. Vasyunina, and S. Yu, "Herschel observations of extraordinary sources: analysis of the full herschel/hifi molecular line survey of sagittarius B2(N)," The Astrophysical Journal 789(1), 8 (2014).
11. J.-C. Loison, "Rate constants and the H atom branching ratio of the reactions of the methylidyne CH(X2Π) radical with C2H2, C2H4, C3H4 (methylacetylene and allene), C3H6 (propene) and C4H8 (trans-butene)," Physical Chemistry Chemical Physics 11(4), 655–664 (2009).
12. J. M. Ribeiro, "Reaction Mechanism and Product Branching Ratios of the CH + C3H6 Reaction: A Theoretical Study," The Journal of Physical Chemistry A 120(11), 1800–1812 (2016).
13. J.-D. Chai, "Long-range corrected hybrid density functionals with damped atom–atom dispersion corrections," Physical Chemistry Chemical Physics 10(44), 6615–6620 (2008).
14. J.-D. Chai, M. Head-Gordon, "Systematic optimization of long-range corrected hybrid density functionals," Physics Chemical Journal 128(8), 084106 (2008).
15. T. H. Dunning, "Gaussian basis sets for use in correlated molecular calculations. I. The atoms boron through neon and hydrogen," The Journal of Chemical Physics 90(2), 1007–1023 (1989).
16. T. B. Adler, "A simple and efficient CCSD(T)-F12 approximation," The Journal of Chemical Physics 127(22), 221106 (2007).
17. G. Knizia, "Simplified CCSD(T)-F12 methods: Theory and benchmarks," The Journal of Chemical Physics 130(5), 054104 (2009).
18. J. M. L. Martin, O. Uzan, "Basis Set Convergence in Secondrow Compounds. The Importance of Core Polarization Functions," Chemical Physics Letters 282(1), 16−24 (1998).
19. J. Zhang, E. F. Valeev, "Prediction of Reaction Barriers and Thermochemical Properties with Explicitly Correlated Coupled-Cluster Methods: A Basis Set Assessment," Journal of Chemical Theory and Computation 8(9), 3175–3186 (2012).
20. M. J. Frisch, G. W. Trucks, H. B. Schegel et al., Gaussian 09 Revision A.1, Gaussian Inc, Wallingford (CT), 66, 219 (2009). [https://gaussian.com].
21. H.-J. Werner, MOLPRO, Version 2010.1, A Package of Ab Initio Programs MOLPRO.NET, University of Cardiff, UK, 2010. [https://www.molpro.net/info/2015.1/doc/manual/index.html].
22. R. A. Marcus, "Unimolecular reactions, rates and quantum state distribution of products," Philosophical Transactions of the Royal Society of London. Series A: Physical and Engineering Sciences 332(1625), 283–296 (1990).
23. P. J. Robinson, K. A. Holbrook, Unimolecular Reactions, Wiley, New York (1972).

24. C. He, L. Zhao, A. M. Thomas, A. N. Morozov, A. M. Mebel, and R. I. Kaiser, "Elucidating the Chemical Dynamics of the Elementary Reactions of the 1-Propynyl Radical (CH3CC; X2A1) with Methylacetylene (H3CCCH; X1A1) and Allene (H2CCCH2; X1A1)," The Journal of Physical Chemistry A 123(26), 5446–5462 (2019).
25. F. Zhang, P. Maksyutenko, and R. I. Kaiser, "Chemical dynamics of the CH (X2Π) + C2H4 (X1A1g), CH (X2Π) + C2D4 (X1A1g), and CD (X2Π) + C2H4 (X1A1g) reactions studied under single collision conditions," Physical Chemistry Chemical Physics 14(2), 529–537 (2012).

Laser Effect on a Pathologically Altered Capsule of the Lens of the Eye

Olga I. Baum[1], Ekaterina M. Kasianenko[1], Alexey V. Yuzhakov[1*], Alibek A. Gamidov[2], Elena P. Medvedeva[2], and Yusef N. Yusef[2]

[1] Institute of Photonic Technologies Federal State Institution "Research Center "Crystallography and Photonics" RAS, 2 Pionerskaya str., Troitsk, Moscow 142190, Russian Federation

[2] Federal State Budgetary Scientific Institution "Research Institute of Eye Diseases", 11 A, B Rossolimo str., Moscow 119021, Russian Federation

*** e-mail:** yuzhalvas@gmail.com

Abstract. One of the current areas of application of lasers in ophthalmology is cataract surgery and reducing the number of negative reactions to surgical intervention. In the postoperative period, clouding of the lens capsular bag and the risk of contraction capsular syndrome associated with changes in the biomechanical properties of the lens and capsular bag system are often observed. In the work, the biomechanics of such system were studied. Lenses that were placed in a 10% formalin solution to create cataract-simulating opacity for various amounts of time were studied by optical-coherent tomography, speckle-interferometry method and with fiber-optics setup for scattering dynamics registration. It was shown that speckle interferometry technique is sensitive to structural changes of lenses due to formalin exposure, which makes tissue more elastic and less transparent. OCT shows the same result and is more sensitive to the changes of laser wavelength. In addition, theoretical studies were carried out and have shown that changing laser wavelength can be dangerous for the integrity of the capsule film during medical intervention due to increase of maximum thermal stress. © 2022 Journal of Biomedical Photonics & Engineering.

Keywords: ophthalmology; cataract simulation; optical diagnostics.

Paper #3480 received 04 Mar 2022; revised manuscript received 05 Apr 2022; accepted for publication 11 Apr 2022; published online 28 Apr 2022. doi: 10.18287/JBPE22.08.020302.

1 Introduction

One of the current areas of application of lasers in ophthalmology is cataract surgery. Despite the obvious progress in the technique of cataract surgery and a decrease in the number of negative consequences, clouding of the lens capsule in the postoperative period is not a rare complication and is detected in a significant percentage of cases [1–4].

The most common complication of laser intervention is transient hypertension of the eye associated with the inflammatory process against the release of prostaglandins in the acute period [5]. To date, there are no clear criteria for selecting laser radiation parameters that guarantee the absence of these complications during laser ablation of a clouded lens capsule, even though that attempts are being made to create algorithms that help to reduce the number of complications associated with laser intervention [6, 7]. As before, to achieve the result, the tactics of stepwise increase in energy to threshold values that allow for cutting the target tissue are more often used.

The variety of clinical and morphological forms of secondary cataracts, which have different optical and mechanical (strength) characteristics, often causes difficulties with the correct calculation of the optimal energy for laser ablation for removing the opacities; it is also the possibility of significant fluctuations in the selected radiation parameters. Errors in the calculation, in this case, also lead to damage to nearby intraocular structures. To a certain extent, the above may be due to gaps in the study of the mechanisms of laser ablation of secondary cataract films when exposed by modulated laser radiation. This indicates the need to continue research in the direction of studying the mechanisms and kinetics of thermomechanical processes during the interaction of laser radiation with multicomponent biological tissues.

The problem of the photodestructive action of lasers on the anatomical structures (Intraocular lens – IOL) of the eye and artificial intraocular elements is the subject of numerous works [8–11], which, in particular, provide data indicating the possibility of developing complications during laser dissection of secondary cataract. In most cases the posterior wall of the lens capsule (PCO) becomes coldly rather than the anterior one. The frequency of opacities in the posterior capsule can vary from 4% to 60% of cases [1, 12], the anterior capsule – 3–16% [13]. Many factors can influence the frequency and severity of "filmy" opacities, among them: age, the presence of concomitant eye, and general diseases, the state of the immunological status and the blood-ocular barrier, the biocompatibility of the IOL and its design features, as well as insufficiently complete removal of the lens masses during the operation, discrepancy between the formed hole in the anterior capsule and the diameter of the IOL [14]. These "filmy" opacities can significantly reduce visual acuity and affect the quality of life, which determines the need for repeated interventions (surgical or laser) in some cases. Unlike surgical interventions, the non-invasive nature of laser operations and the possibility of strict dosing of the energy parameters of the radiation make it possible to achieve high functional results and to repeat the procedure if necessary. At the same time, to determine the most effective mode of laser exposure, knowledge of the properties of the lens and capsular system is necessary.

Recently, methods for non-invasive determination of the mechanical properties of eye tissues are of particular interest. In recent years, it has been shown that the elastic properties of tissues measured at different depths can serve as a kind of marker of pathology, which is not inferior to traditional histological techniques in terms of selectivity [15–18]. In this direction, the method of optical coherent elastography (OCE) has been widely developed, the resolution of which is significantly superior to the method of ultrasound diagnostics and most other methods of medical imaging [17–19]. The high resolution of the OCE method in terms of the analysis time makes it possible to visualize the dynamics of deformations in the tissues of the eye during millisecond laser pulses [20].

This work is related to the development of the scientific foundations of a new laser method of exposure to "filmy" opacities in the pupil area, including both opacities of the posterior lens capsule (PCO) and anterior, accompanied by progressive contraction of the capsule (anterior capsular contraction syndrome – ACCS), leading to deformation IOL. The optical properties of the anterior and posterior lens capsules are directly related to their biomechanical properties, which affect the absorption of laser radiation in the considered range. Thus, the study of the biomechanical properties of intraocular structures and their dynamics under the influence of laser radiation can provide new information for the correction of laser modes of exposure in order to minimize side effects associated with laser ophthalmological operations. This paper presents a theoretical study of the effect of various parameters of laser exposure on thin biological films of the lens capsule, modified and intact, as well as a study of the biomechanics of the lens and capsular system, which can further help in more accurate control of the temperature and thermal stress fields during laser exposure at surgical operation.

2 Materials and Methods

2.1 Theoretical Study

The temperature field was calculated, based on the modernization of the theoretical model that describes the laser effect on the volume of biological tissue, taking into account the propagation of heat by thermal conduction, and also taking into account the attenuation of laser radiation with depth in accordance with the Bugger-Lambert-Beer law [21, 22], depending on the temporal (pulse-periodic) pattern of laser exposure and its intensity, allowing at any moment of the considered time to obtain a temperature distribution within the lens capsule volume.

The geometry of the problem took into account that the laser radiation was delivered through an optical fiber 600 μm in diameter, which was inserted into the biological sample perpendicular to its surface. The problem of heat propagation by thermal conductivity under laser irradiation at wavelengths of 1560 nm and 1450 nm was solved. The distinction between these variants of exposure consisted in different absorption of laser radiation by biotissue. So, as an absorption index for a wavelength of 1560 nm in numerical simulation, the value of 10 cm^{-1} was chosen, and for 1450 nm – the value of 33 cm^{-1}. The intensity profile at the output of the fiber was taken as a Gaussian distribution with an effective Gaussian radius of 250 μm for a fiber end diameter of 600 μm. In order for further experiments using the method of optical coherent elastography to be able to isolate the effect of only one laser pulse, without taking into account the influence of residual oscillations from previous pulses, a repetitively pulsed mode was chosen for numerical simulation with a pulse duration of 100 ms, and a 1900 ms pause between pulses, irradiation duration 20 s. The values of the laser irradiation power were chosen in such a way that tissue denaturation was not achieved and, at the same time, the amplitudes of tissue oscillations obtained experimentally by the OCE method exceeded the noise by an order of magnitude. For the selected modes, both the dynamics of the maximum temperature at each moment of time and the profiles of the temperature field for the capsule film were constructed. The calculation scheme took into account the introduction of an optical fiber into the lens capsule and irradiation of the capsule film from the inside. Laser-induced thermal stresses corresponding to the difference between the angular and radial components of the stress tensor, arising along the capsule surface, perpendicular to the radiation axis due to uneven heating in this direction,

can be calculated using the formulas given in Refs. [22, 23].

2.2 Experimental Study

The study plan was approved by the local ethics committee. All procedures followed were consistent with the principles set out in the 1975 Declaration of Helsinki and its 2000 revision.

(1) Modeling Technique of Lens Capsule Opacities Using Formalin

The experiment used isolated pig eyes obtained from a slaughterhouse. The isolated eyes were stored in a refrigerator (+4 °C) in a physiological solution of 0.9% NaCl for no more than a day. After removal from the eyeballs, the lenses were immediately placed in a 10% formalin solution to create cataract-simulating opacity. The modification was carried out for 60 min with checkpoints at 15, 30, and 60 min. Obtaining a visual picture of lens changes was carried out using an Amoeba Celestron Microscope 44325 microscope.

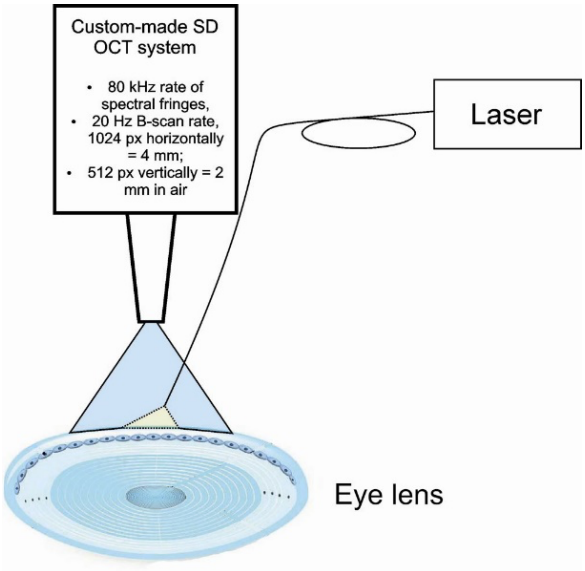


Fig. 1 Scheme of irradiation of a lens and simultaneous recording of OCE.

(2) Optical Coherent Elastography

For the subsequent study of the biomechanics of the modified and intact lens and capsular system and the influence of various laser parameters on it, experiments were carried out to determine the dynamics of thermo-elastic strains using OCE with simultaneous irradiation of the system in the selected modes. We used an OCT elastography method, previously used to study eye tissues [23–25], created at the Institute of Applied Physics, Russian Academy of Sciences, Nizhny Novgorod, by a group led by V. Yu. Zaitsev, with an imaging area of 4 mm wide and 2 mm deep, the setup made it possible to obtain the dependence of internal strains on time at a rate of 80 kHz for spectral bands and 20 Hz for B-scans.

The study of the response of the anterior and posterior capsules to a laser pulse during cataract modeling using formalin was carried out at two wavelengths of 1560 and 1450 nm. Tissue irradiation was carried out at different powers in two repetitively pulsed modes:

1. Wavelength 1.56 μm, pulse duration 100 ms, pause between pulses 1900 ms.
2. Wavelength 1.45 μm, pulse duration 100 ms, pause between pulses 1000 ms.

(3) Experiments on the Dynamics of Scattering and Transmission of Low-Intensity Scanning Laser Radiation

To carry out experiments on the dynamics of scattering and transmission of low-intensity scanning laser radiation, a scheme of a fiber-optic system was used (Fig. 2). The laser radiation was delivered through an optical "output" fiber 600 μm in diameter, inserted into the biological sample perpendicular to its surface through which the radiation passed. Beyond the sample surface, coaxially with the output optical fiber that supplied radiation to the sample, there was a "receiving" optical fiber connected to an optical multichannel analyzer in which the signal was digitized. Irradiation of the surface of each lens was carried out 4 times.

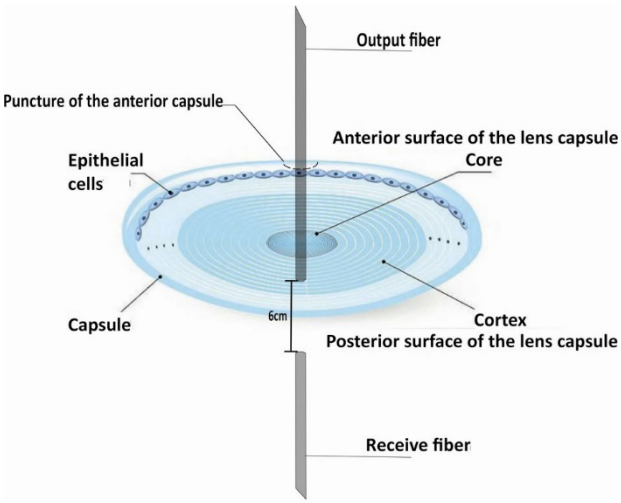


Fig. 2 Scheme of irradiation of the lens capsule and receiving optical fiber for detecting the transmitted signal.

The geometry and power of both visualizing and heating radiation were the same in all four-irradiation series. The wavelength of scanning radiation is 0.53 μm (visible range), heating 1.56 μm. Irradiation was carried out in a repetitively pulsed mode with a pulse duration of 100 ms and a pause between pulses of 1900 ms, the total duration of irradiation was 20 s (10 exposure peaks were obtained in total), the power was 0.3 W and 0.5 W.

(4) Speckle-Interferometry

Previously, we have already studied the relationship between the data obtained by the OCE method and the data of speckle interferometry [23]. In the present work, the irradiation mode corresponded to the chosen mode for experiments with the transmission of scanning radiation. The scheme of the setup for studying speckle interferometry is shown in Fig. 3. The radiation was delivered through an optical fiber with a diameter of 600 μm, directed at an angle of 15° to the normal. Simultaneously with heating, the sample was illuminated with a wide beam of a helium-neon laser with an angle of incidence of 45°. The probe beam, reflected normal to the sample, is captured by a 2D camera (Videozavr, VZ-M50S, 1296 × 972 pixels, 21 frames/s) to acquire an image and track changes in the statistical properties of speckle structures caused by heating.

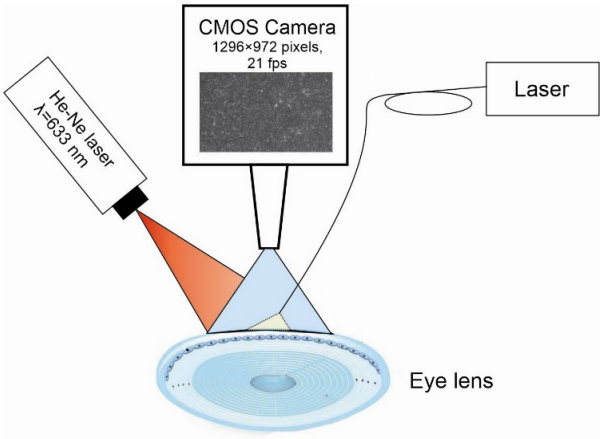


Fig. 3 Scheme of a speckle imaging setup.

The obtained images were used to calculate the statistical functions of the speckle patterns, such as the average light intensity and the Pearson cross-correlation coefficient (decorrelation function).

3 Results and Discussion

Numerical simulation for a power of 0.5 W, for a wavelength of 1560 nm made it possible to obtain at the first peak of exposure the maximum temperature change of 20.8 °C relative to the initial temperature, while at the last peak this value reached 22.2 °C.

Due to the thickness of the capsule film of a young healthy person of 11–18 μm and temperature difference of 0.20 ± 0.02 °C between boundary planes of capsule film during the pulse it can be assumed that heating is even along the radiation axis. Numerical simulation has shown that in the capsule layer at the first irradiation peak, the temperature profile can be approximated by one normal distribution, while at the last irradiation peak – by the sum of two normal distributions, one of which takes into account the propagation of heat perpendicular to the radiation axis due to thermal conductivity, and the dispersion of these two distributions differ by a factor of 20. Laser-induced thermal stresses in the lens capsule at the first and 20 peaks of laser radiation at a wavelength of 1560 nm are shown in Fig. 4.

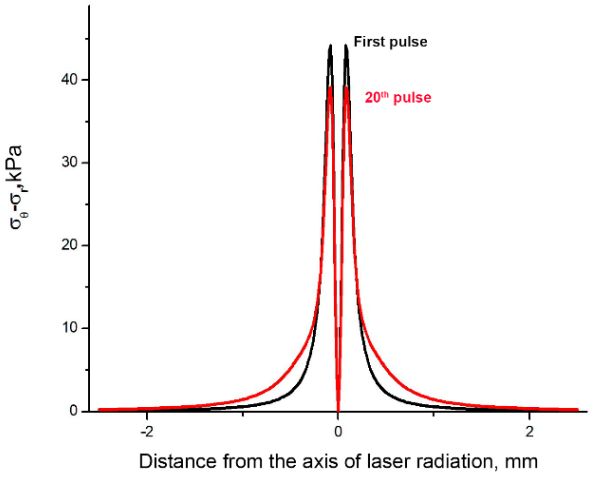


Fig. 4 Laser-induced thermal stresses in the lens capsule at the first and twentieth peaks of laser radiation at a wavelength of 1560 nm.

A similar calculation for a wavelength of 1450 nm showed that a decrease in the absorption depth by 3 times leads to the fact that at the first peak of exposure the maximum temperature change relative to the initial temperature was 55.7 °C, while at the last peak this value reached 59.7 °C. At the same time, in the capsule film, the temperature drop was 1.8 ± 0.2 °C, and the thermal stresses were 4 times greater than for a wavelength of 1560 nm, which can be dangerous for its integrity during medical intervention and can lead to additional wrinkling and the appearance of cavities and spaces in which the process of proliferation of lens epithelial cells can begin. Thus, for the subsequent experimental study with the human eye, we should choose a wavelength of 1560 nm, while in this work both wavelengths of laser radiation were used to treat pig's eyes.

3.1 Study of Visual Changes in the Structure of the Formalin-Modified Lens

As a result of a visual assessment, it was found that opacities of the lens are observed already after 15 min from placing it in formalin. Noticeable opacities with compaction of the surface layers of the lens, namely its capsule, increases with increasing exposure to soaking in a formalin solution, which is clearly seen in the presented photographs. Possibility of experimental modeling of postoperative opacification of the lens capsule of different intensity correlates with different types of opacities of the lens capsule after real cataract surgery. This makes it possible to solve applied problems of selecting the optimal parameters of laser radiation during laser dissection of secondary cataract films with different optical densities.

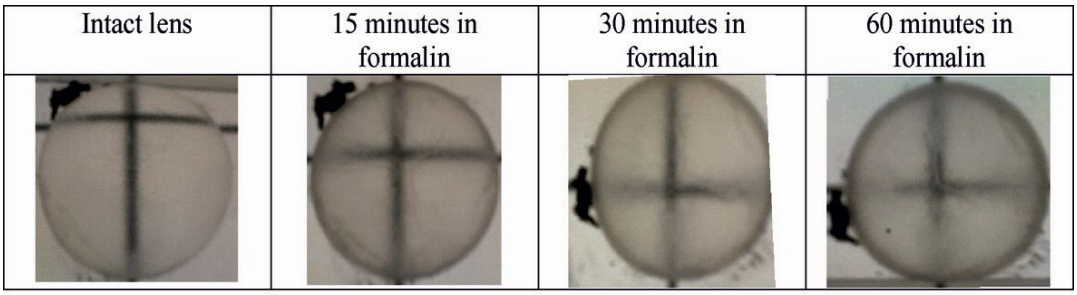
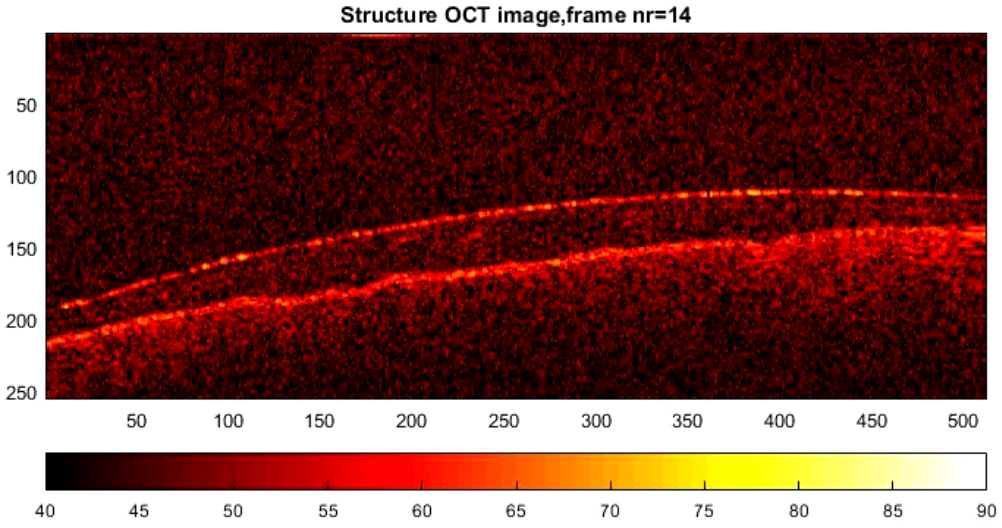
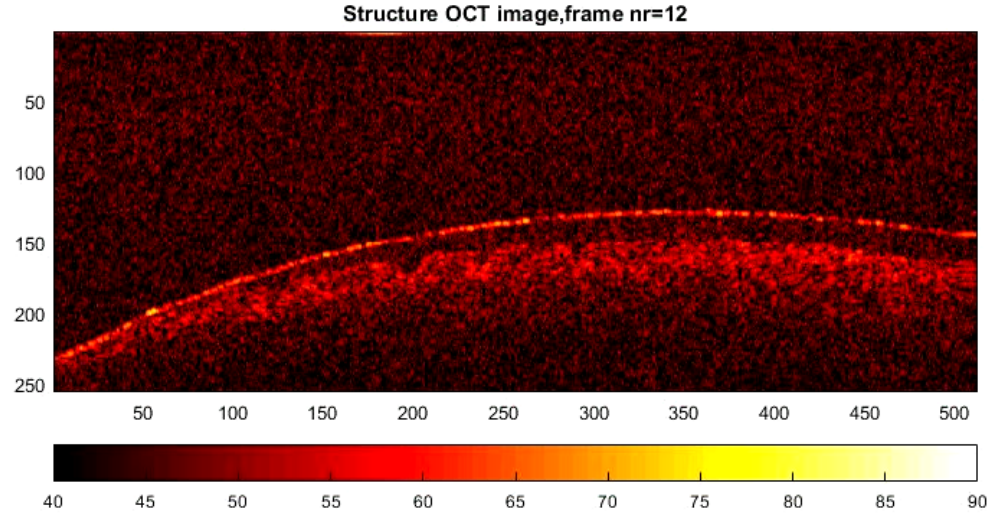


Fig. 5 Photographs of the capsule + lens system, with structure modification using formalin soak for various times for visual evaluation.



(a)



(b)

Fig. 6 OCE structural image (a) of the anterior and (b) of the posterior surface of the lens of the eye 30 min after they were exposure in formalin.

3.2 Study of Structural Changes Using OCE

The OCE setup made it possible to obtain structural images of the capsule surface area for the isolated porcine lens (Fig. 6). The evaluation was carried out on both sides of the modified porcine lens (anterior and posterior) along the center line.

When examining the intact lens tissue, it was noticed that for the anterior capsule there is a separation of the structure in the superficial layers with a very thin distance

between them, for the posterior surface such separation was not observed.

Cataract modeling by placing the lens in formalin for 30 min or more led to the following changes in OCE images of the structure:

- For the anterior surface of the lens, in 60% of cases there was a significant increase in the distance between the surface (capsule) and the contents (inner layers and nucleus) of the lens. In other cases, an increase in this distance was also observed, however, not so significant.
- For the posterior surface, a discernible separation of the surface was observed in only 30% of cases.

It is important to note that this ratio appeared already after 15 min of exposure in formalin and was maintained regardless of the duration of exposure.

3.3 Evaluation of Surface Subsidence under Laser Exposure

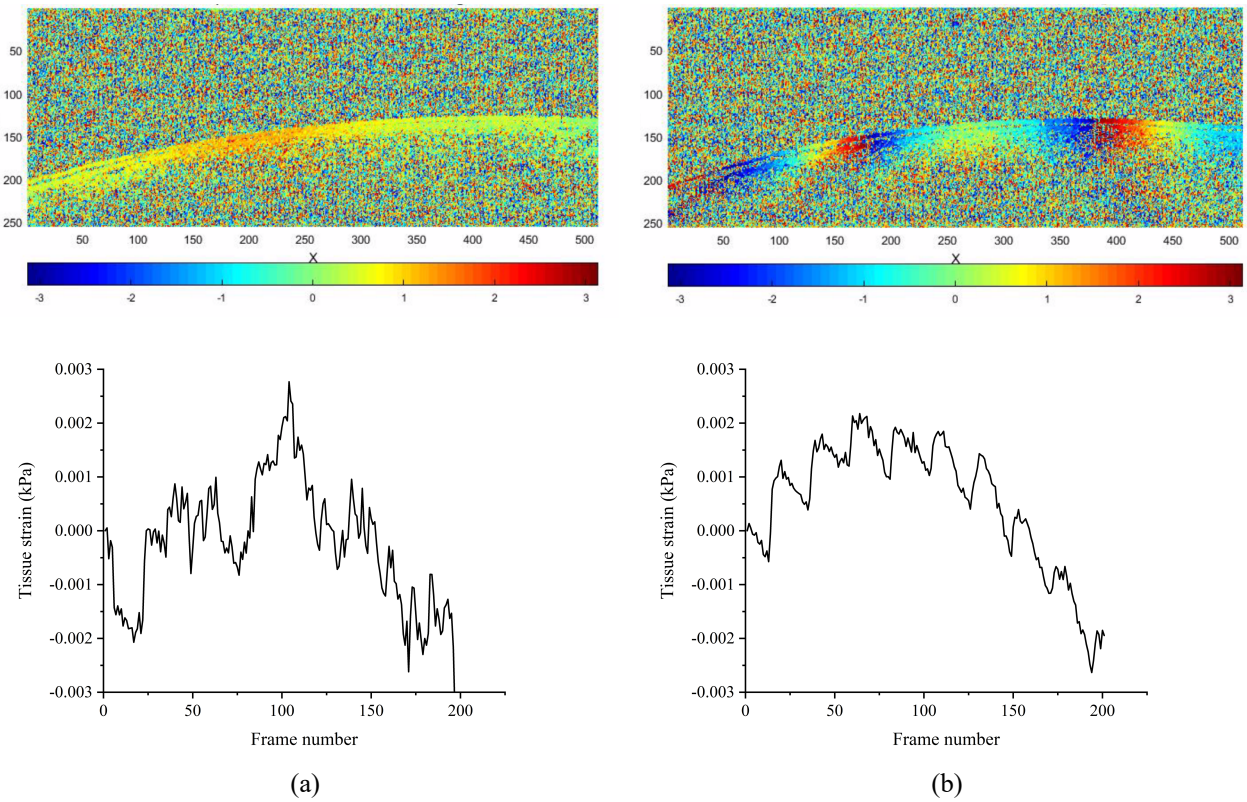
Evaluation of the change in the height of the position of the sample surface along the central axis under laser irradiation was carried out using OCE structural images of the lens. For this, three frames were compared: the moment before the first laser pulse, the moment before the last laser pulse, and the moment 50 frames after the last laser pulse.

As a result, it was found that surface subsidence under laser irradiation does not occur for all samples. The surface of the anterior lens capsule of intact samples, and samples after being placed in formalin for 15 and 30 min experienced obvious subsidence after exposure to laser radiation with a wavelength of 1.45 μm. Moreover, the amount of sedimentation did not depend on the type of sample and the duration of its exposure in formalin. A similar laser impact on the posterior lens capsule did not cause its subsidence for both intact and formalin-modified samples.

Under laser action with a wavelength of 1.56 μm, a completely different behavior of the samples was observed. Surface settling did not occur during irradiation of the posterior or anterior lens capsule, either for intact specimens or for 15 min formalin-modified samples. However, for samples after 30 min exposure in formalin, subsidence of the surface of the posterior lens capsule was observed, while no subsidence occurred during laser exposure to the anterior capsule.

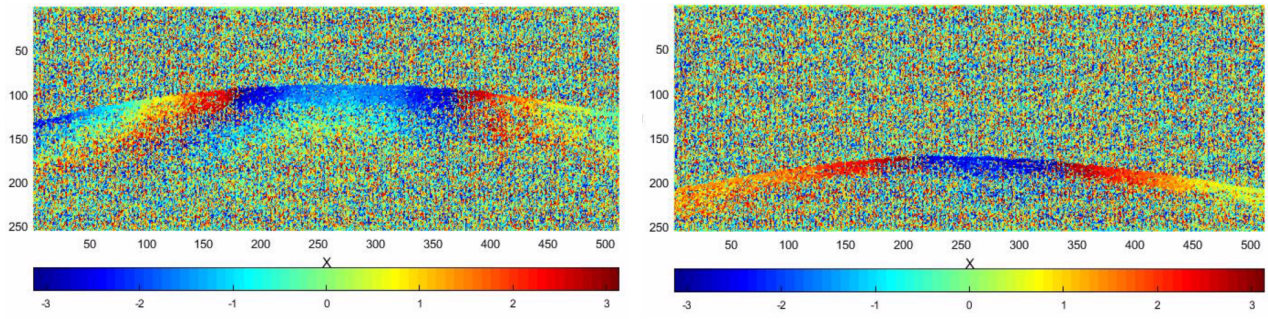
3.4 Deformation Response under Laser Action

A different pattern of deformations was observed for the formalin-modified lenses under the laser radiation with different wavelengths. Thus, for the anterior lens capsule (Fig. 7), radiation with a wavelength of 1.56 μm practically did not create any deformation patterns either on the surface or in the body of the sample.



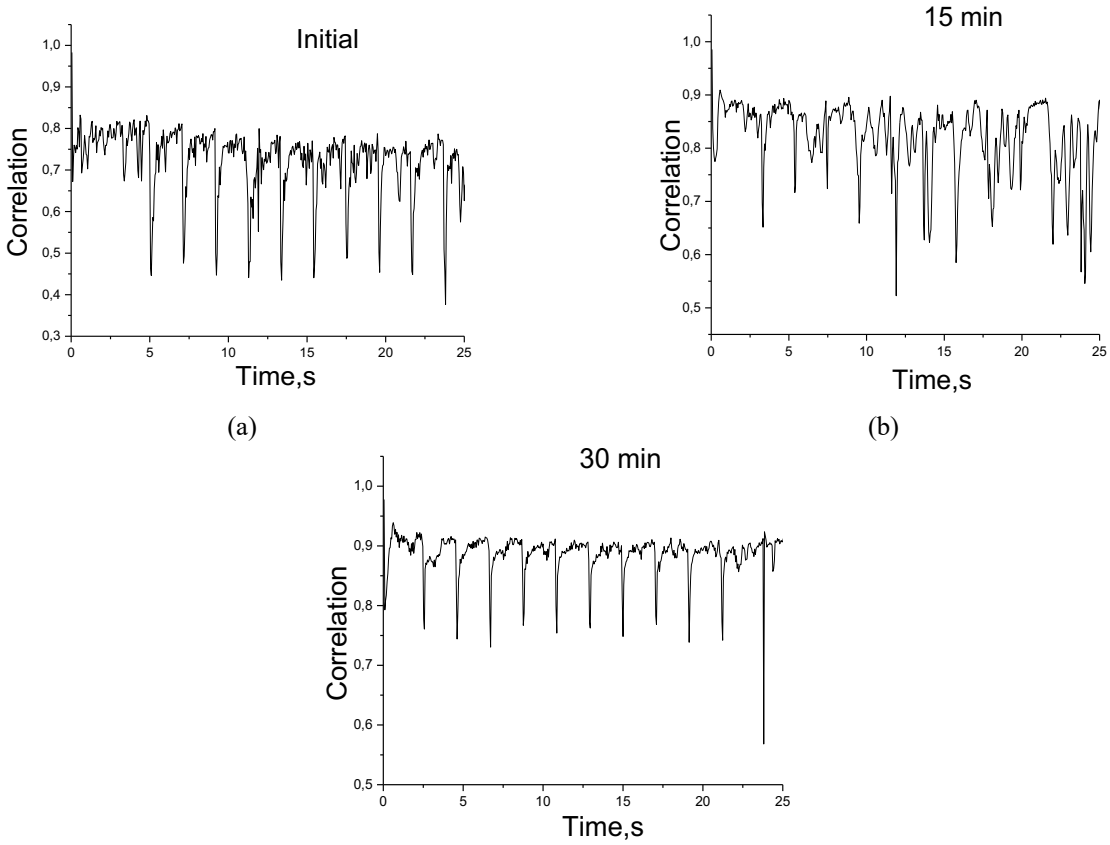
(a) (b)

Fig. 7 Interframe phase difference and time dependence of tissue strain on the anterior capsule during laser exposure to the 15 min formalin-modified lens of the eye. Wavelength of laser radiation: (a) 1.56 μm; (b) 1.45 μm.



(a) (b)

Fig. 8 Interframe phase difference on the posterior capsule during laser exposure to the 15 min formalin-modified lens of the eye. Wavelength of laser radiation: (a) 1.56 μm; (b) 1.45 μm.



(a) (b)

(c)

Fig. 9 Decorrelation of the speckle-interferometric pattern of the porcine lens for different modification times in formalin: (a) before modification, (b) 15 min of modification, (c) 30 min of modification.

And for a wavelength of 1.45 μm, significant tissue deformations were observed throughout its depth, and the relaxation time of these deformations was much longer: 2 ± 1 frame at a wavelength of 1.56 μm for the first pulse versus 5 ± 1 frame for wavelength 1.45 μm. For the last laser pulse, the duration was 4 ± 1 and 6 ± 2 frames, respectively. Fig. 7 demonstrates interframe phase difference and time dependence of tissue strain on the anterior capsule during laser exposure to the 15 min formalin-modified lens of the eye. To determine the tissue strain value, an area along the axis of laser exposure immediately below the surface of the lens was chosen. From the graphs, the reaction of the anterior capsule to laser exposure with a wavelength of 1.45 μm is well defined, while for a wavelength of 1.56 μm, it is impossible to determine the moments of laser exposure from the graph of time dependence of tissue strain. For the posterior lens capsule, the graphs of time dependence of tissue strain also do not show an obvious response of the tissue strain amplitude to laser exposure.

From the pattern of deformation on the anterior (Fig. 7) and posterior (Fig. 8) lens capsules, the results of the assessment of surface subsidence given above become clear. Obviously, laser radiation with a wavelength of 1.45 μm has a greater effect on the structures of the anterior lens capsule.

3.5 Study of Changes in the Structure of the Lens in the Capsular Bag of the Eye when Placed in Formalin by Speckle Interferometry

Using the speckle interferometry method, videos of the surface of the porcine lens under laser exposure were obtained and processed. Fig. 9 shows the dependences of the decorrelation function on time under the influence of laser pulses for different residence times in formalin.

The relative drop in the value of the cross-correlation coefficient with laser pulses was estimated. The results are presented in Fig. 10.

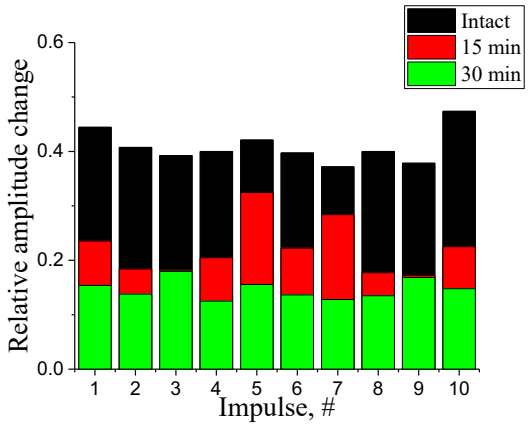


Fig. 10 Relative change in the decorrelation of the speckle interferometric pattern of the porcine lens for different modification times in formalin in response to laser pulses.

A comparison of the relative amplitudes of individual irradiation peaks for the same capsule sample showed that the relative amplitude of the peaks from the intact sample is higher than for the modified ones. At the same time, it was noted that the amplitude decreases with an increase in the time of modification of the capsule in the formalin solution, that is, with an increase in the number of crosslinks in the biological tissue, which make the sample more elastic and less transparent.

3.6 Study of the Change in the Scattering of the Lens of the Eye When Placed in a Formalin Solution

An experiment was carried out on the lenses of a pig to assess the effect of the irradiation wavelength on the response of tissue under laser irradiation. Fig. 11 shows the time dependences of the transmitted radiation for the lens of the pig's eye for wavelengths of 1.45 μm and 1.56 μm.

According to the results obtained, it can be seen that when irradiated with a wavelength of 1.56 μm, the film does not accumulate structural changes caused by laser heating, and for 1.45 μm, the transmission decreases significantly. Such an effect can be caused by the difference in absorption coefficients for these wavelengths in water, which is the main absorber in this tissue (10 cm^{-1} for 1.56 μm and 33 cm^{-1} for 1.45 μm).

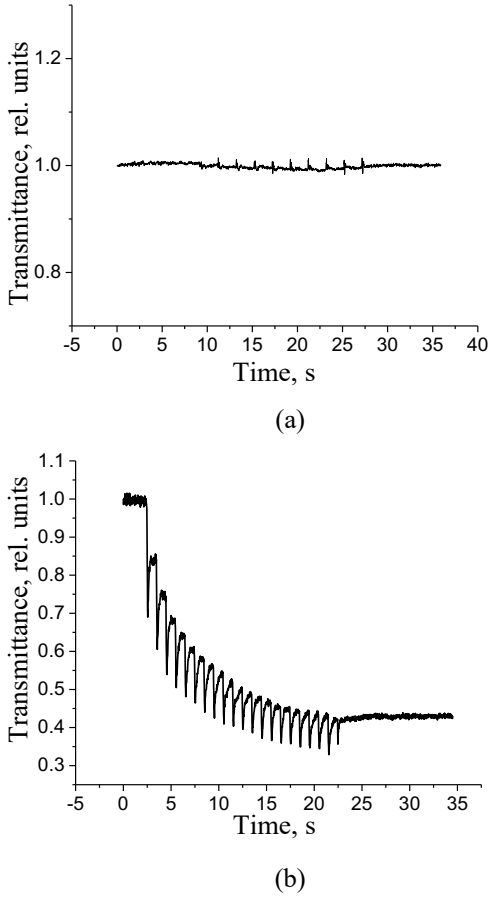


Fig. 11 Transmission of laser radiation for the posterior film of the lens, exposed in formalin for 60 min, for wavelengths (a) 1.56 μm and (b) 1.45 μm.

4 Conclusions

Noticeable opacity with compaction of the surface layers of the lens, namely its capsule, increases with increasing exposure time in formalin solution, which creates the possibility of experimental modeling of postoperative opacification of the lens capsule of varying intensity, and correlates with various types of opacities of the lens capsule after real cataract surgery. This makes it possible to solve applied problems of selecting the optimal parameters of laser radiation during laser dissection of secondary cataract films with different optical densities.

At the same time, for the anterior surface of the lens, in 60% of cases there is a significant increase in the distance between the surface (capsule) and the contents (inner layers and core) of the lens. For the posterior surface, a discernible separation of the surface is observed only in 30% of cases. These changes occur during the first 15 min of exposure to formalin and then persist regardless of the exposure time.

The speckle interferometry technique is sensitive to this modification of a biological tissue, since the relative amplitude of the correlation peaks of the speckle interferometric pattern from an intact sample is higher than for modified ones, and it decreases with increasing

exposure time, that is, with an increase in the number of crosslinks in a biological tissue that make the sample more elastic and less transparent.

The OCE technique can also detect the modification of biological tissue and, at the same time, this method is sensitive to changes in the wavelength of laser exposure.

For the selected exposure parameters, it was shown that a decrease in the absorption depth by a factor of 3 led to an increase in the maximum thermal stress by a factor of 4, which can be dangerous for the integrity of the capsule film during medical intervention.

Disclosures

All authors declare that there is no conflict of interests in this paper.

Acknowledgements

The work was supported by the Ministry of Science and Higher Education of the Russian Federation within the framework of the State task of the Federal Research Center "Crystallography and Photonics" of the Russian Academy of Sciences in part of a theoretical study of the dynamics of laser exposure processes during laser destruction of the lens capsule and OCT study of structural changes, as well as by the Russian Foundation for Basic Research (project No. 20-02-00486) in terms of *ex vivo* studies of intact and modified biological tissues.

References

1. N. P. Pashtaev, I. V. Kulikov, "Femtosecond laser in cataract surgery," The Fyodorov Journal of Ophthalmic Surgery 3, 74–79 (2016) [in Russian].
2. R. Autrata, J. Rehůrek, "Intraocular lens implantation in children," Ceska a Slovenska Oftalmologie: Casopis Ceske Oftalmologicke Spolecnosti a Slovenske Oftalmologicke Spolecnosti 56(5), 303–310 (2000).
3. D. Baráková, P. Kuchynka, D. Klecka, J. Simůnková, and J. Borovanská, "Frequency of secondary cataracts in patients with AcrySof MA30BA and MA60BM lenses," Ceska a Slovenska Oftalmologie: Casopis Ceske Oftalmologicke Spolecnosti a Slovenske Oftalmologicke Spolecnosti 56(1), 38–42 (2000).
4. J. R. Shepherd, Complications of foldable implants, ASCRS, Boston (STAAR Surg. Inc.) (1997).
5. A. Parajuli, P. Joshi, P. Subedi, and C. Pradhan, "Effect of Nd: YAG laser posterior capsulotomy on intraocular pressure, refraction, anterior chamber depth, and macular thickness," Clinical Ophthalmology (Auckland, NZ) 13, 945 (2019).
6. A. A. Gamidov, A. V. Bol'shunov, A. V. Yuzhakov, E. M. Shcherbakov, O. I. Baum and E. N. Sobol, "Optical transmission and laser ablation of pathologically changed eye lens capsule," Quantum Electronics 45(2), 180–184 (2015).
7. O. I. Baum, O. G. Romanov, A. A. Gamidov, A. A. Fedorov, G. S. Romanov, G. I. Zheltov, and E. N. Sobol, "Optimization of laser surgery of the secondary cataract," Almanac of Clinical Medicine 44(2), 130–139 (2016) [in Russian].
8. G. I. Zheltov, "Problems of safety when working with lasers," Ophthalmology in Belarus 4, 39–45 (2010) [in Russian].
9. F. Fankhauser, S. Kwasniewska (Eds.), Lasers in Ophthalmology: Basic, Diagnostic and Surgical Aspects: A Review, Kugler Publications, The Hague (2003).
10. L. E. Katz, J. A. Fleischman, and S. L. Trokel, "The YAG laser: an American experience," American Intra-Ocular Implant Society Journal 9(2) 151–156 (1983).
11. A. A. Gamidov, V. V. Sosnovskiĭ, V. I. Boev, and M. A. Buzykanova, "Study of risk factors of laser irradiation-induced intraocular lens damage," Vestnik Oftalmologii 122(5), 28–31 (2006).
12. D. Baráková, P. Kuchynka, D. Klecka, J. Simůnková, and J. Borovanská, "Frequency of secondary cataracts in patients with AcrySof MA30BA and MA60BM lenses," Ceska a Slovenska Oftalmologie: Casopis Ceske Oftalmologicke Spolecnosti a Slovenske Oftalmologicke Spolecnosti 56(1), 38–42 (2000).
13. A. A. Gamidov, Laser reconstructive interventions in the area of the iridolenticular diaphragm in pseudophakia (clinical and experimental study), Doctor of sciences thesis, Moscow (2016) [in Russian].
14. R. F. Steinert, "Neodymium: Yttrium-Aluminum-Garnet Laser Posterior Capsulotomy," Chapter 51 in Cataract Surgery, 3rd ed., Philadelphia, Elsevier, WB Saunders, 617–629 (2009).
15. E. V. Gubarkova, A. A. Sovetsky, V. Yu. Zaitsev, A. L. Matveyev, D. A. Vorontsov, M. A. Sirotkina, L. A. Matveev, A. A. Plekhanov, N. P. Pavlova, S. S. Kuznetsov, A. Yu. Vorontsov, E. V. Zagaynova, and N. D. Gladkova, "OCT-elastography-based optical biopsy for breast cancer delineation and express assessment of morphological/molecular subtypes," Biomedical Optics Express 10(5), 2244–2263 (2019).
16. K. J. Parker, M. M. Doyley, and D. J. Rubens, "Imaging the elastic properties of tissue: the 20 year perspective," Physics in Medicine & Biology 56(1), R1–R29 (2011).

17. K. M. Kennedy, R. A. McLaughlin, B. F. Kennedy, A. Tien, B. Latham, C. M. Saunders, and D. D. Sampson, "Needle optical coherence elastography for the measurement of microscale mechanical contrast deep within human breast tissues," Journal of Biomedical Optics 18(12), 121510 (2013).
18. S. Wang, K. V. Larin, "Optical coherence elastography for tissue characterization: a review," Journal of Biophotonics 8(4), 279–302 (2015).
19. V. Y. Zaitsev, A. L. Matveyev, L. A. Matveev, A. A. Sovetsky, M. S. Hepburn, A. Mowla, and B. F. Kennedy, Strain and elasticity imaging in compression optical coherence elastography: The two-decade perspective and recent advances," Journal of Biophotonics 14(2), e202000257 (2021).
20. V. Y. Zaitsev, A. L. Matveyev, L. A. Matveev, G. V. Gelikonov, A. I. Omelchenko, O. I. Baum, S. E. Avetisov, A. V. Bolshunov, V. I. Siplivy, D. V. Shabanov, A. Vitkin, and E. N. Sobol, "Optical coherence elastography for strain dynamics measurements in laser correction of cornea shape," Journal of Biophotonics 10(11), 1450–1463 (2017).
21. O. I. Baum, G. I. Zheltov, A. I. Omelchenko, G. S. Romanov, O. G. Romanov, and E. N. Sobol, "Thermomechanical effect of pulse-periodic laser radiation on cartilaginous and eye tissues," Laser Physics 23(8), 085602 (2013).
22. O. I. Baum, A. V. Yuzhakov, A. V. Bolshunov, V. I. Siplivyi, O. V. Khomchik, G. I. Zheltov, and E. N. Sobol, "New laser technologies in ophthalmology for normalisation of intraocular pressure and correction of refraction," Quantum Electronics 47(9), 860 (2017).
23. O. I. Baum, V. Y. Zaitsev, A. V. Yuzhakov, A. P. Sviridov, M. L. Novikova, A. L. Matveyev, L. A. Matveev, A. A. Sovetsky, and E. N. Sobol, "Interplay of temperature, thermal-stresses and strains in laser-assisted modification of collagenous tissues: Speckle-contrast and OCT-based studies," Journal of Biophotonics 13(1), e201900199 (2020).
24. V. Y. Zaitsev, A. L. Matveyev, L. A. Matveev, G. V. Gelikonov, A. I. Omelchenko, O. I. Baum, S. E. Avetisov, A. V. Bolshunov, V. I. Siplivy, D. V. Shabanov, A. Vitkin, and E. N. Sobol, "Optical coherence elastography for strain dynamics measurements in laser correction of cornea shape," Journal of Biophotonics 10(11), 1450–1463 (2017).
25. V. Y. Zaitsev, A. L. Matveyev, L. A. Matveev, A. A. Sovetsky, O. I. Baum, A. V. Yuzhakov, A. I. Omelchenko, and E. N. Sobol, "OCT-based strain mapping and compression optical coherence elastography to study and control laserassisted modification of avascular collagenous tissues," Proceedings of SPIE 11242, 1124202 (2020).

Optical Properties of Glycated and Non-Glycated Hemoglobin – Raman/Fluorescence Spectroscopy and Refractometry

Ekaterina N. Lazareva[1,2*], Andrey Y. Zyubin[3], Natalya I. Dikht[4], Alla B. Bucharskaya[1,2,4], Ilya G. Samusev[3], Vasily A. Slezhkin[3,5], Vyacheslav I. Kochubey[1,2], and Valery V. Tuchin[1,2,6]

[1] Science Medical Center, Saratov State University, 83 Astrakhanskaya str., Saratov 410012, Russia

[2] Laboratory of Laser Molecular Imaging and Machine Learning, Tomsk State University, 36 Lenin av., Tomsk 634050, Russia

[3] REC "Fundamental and Applied Photonics. Nanophotonics", Immanuel Kant Baltic Federal University, 14A Nevskogo str., Kaliningrad 236041, Russia

[4] Saratov State Medical University named after V. I. Razumovsky, 112 Bolshaya Kazachia str., Saratov 410012, Russia

[5] Department of Chemistry, Kaliningrad State Technical University, 1 Sovietsky prospect, Kaliningrad 236022, Russia

[6] Laboratory of Laser Diagnostics of Technical and Living Systems, Institute of Precision Mechanics and Control, FRC "Saratov Research Centre of the Russian Academy of Sciences", 24 Rabochaya str., Saratov 410028, Russia

*** e-mail:** LazarevaEN@list.ru

Abstract. In this study, the optical properties of glycated (HbA1c) and non-glycated (Hb) hemoglobin are compared using Surface-enhanced Raman spectroscopy (SERS), spectrofluorimetry, and refractometry. Analysis of the spectral shift of SERS spectra showed good discrimination between two hemoglobins indicating differences in their molecular structure. The fluorescence spectra measured at excitation wavelengths of 260, 270, and 280 nm also indicate differences in the molecular structure of these hemoglobins. For the first time refractive index temperature increments were measured for HbA1c in a wide wavelength range in the visible and NIR as $-(1.35 \pm 0.11) \times 10^{-4}\,°C^{-1}$ and compared with normal hemoglobin ($dn/dT = -(1.02 \pm 0.12) \times 10^{-4}\,°C^{-1}$). The comparison of temperature RI increments for hemoglobin obtained from the whole blood of healthy volunteers and diabetic patients is also done. The data obtained can serve as a basis for further study of the optical properties of glycated hemoglobin and other glycated proteins. © 2022 Journal of Biomedical Photonics & Engineering.

Keywords: refraction; refractive index; temperature increment; fluorescence; Raman spectroscopy; SERS; hemoglobin; glycated hemoglobin HbA1c.

Paper #3479 received 28 Feb 2022; revised manuscript received 25 Apr 2022; accepted for publication 25 Apr 2022; published online 14 May 2022. doi: 10.18287/JBPE22.08.020303.

1 Introduction

According to current statistical data, the incidence of diabetes mellitus is increasing every year. Among methods of diagnostics are methods based on the quantitative determination of glycated proteins, which are biological markers of the disease [1–3]. One of them that is often used as a marker is HbA1c which is formed by the nonenzymatic glycation of hemoglobin exposed to free blood glucose and therefore has a strong correlation with the average glucose concentration in the bloodstream in the preceding three-month period (life span of the erythrocytes). Because of this strong correlation, HbA1c levels have been regularly used to monitor long-term glucose control in established diabetics and have been recently approved for screening for diabetes ($HbA1c \geq 6.5\%$) and prediabetes ($5.7\% \leq HbA1c \leq 6.4\%$) [1–6].

Currently, there are more than 20 methods for the determination of glycated hemoglobin, such as cation exchange chromatography, electrophoresis, affinity chromatography, and immunoassay, but each of them measures various fractions of glycated hemoglobin [1–3]. Most of the methods used are based on the chemical separation of the non-glycated and glycated hemoglobin fractions and the subsequent determination of the concentration of glycated hemoglobin by subtracting the unbound form from the total amount of hemoglobin. These methods are invasive and have significant drawbacks, for example, chromatography is very sensitive to changes in temperature and pH [2].

At present, optical methods represent ample opportunities and are promising for the development of rapid and non-invasive methods of diagnosis and therapy of early stages of diseases such as diabetes, cancer, and others [7–11]. Knowledge of the optical properties of blood, hemoglobin, glycated hemoglobin, and its distinctive features will help in developing a quick, simple, and noninvasive method for diagnosing these diseases. For example, *in vivo* flow cytometry of diabetic patients with melanoma may have additional background signals from glycated erythrocytes [7].

In this paper, a comparative analysis of the optical properties of glycated and normal hemoglobin was performed by using refractometry, spectrofluorimetry and Surface-enhanced Raman spectroscopy (SERS). Optical methods chosen in this study are most often used as diagnostic techniques and allow for detection of substances by differences in their molecular structure [12–14]. Raman spectroscopy (RS) is widely used as a powerful diagnostic tool in biomedical research due to the possibility to provide fingerprint information of the molecular composition and structure of a sample, such as proteins, lipids, etc. [15]. For diabetes diagnosis, Han et al. [16] used RS to analyze the serum of diabetic patients as Barman et al. [17] used it to detect the glycated hemoglobin in hemolysate model formed by two-component mixture (Hb and HbA1c) [16, 17]. As an alternate method for HbA1c detection, Ishikawa and co-workers have recently reported the application of Surface-enhanced resonance Raman spectroscopy (SERRS) [18]. Although promising in approach, precise quantification of the analyte of interest (HbA1c) using SERRS is difficult (as also was noted by the authors), because of poor spectral reproducibility and the generation of spurious background signals [19]. The use of RS allows for a qualitative analysis of the samples and clarifies the results obtained by refractometric and fluorescent methods. It has been shown the possibility of SERRS to identify the distinctive features of glycated forms of proteins (albumin, hemoglobin) from non-glycated [14, 20, 21]. Native fluorescence spectroscopy of blood plasma in rats with experimental diabetes was used to identify the characteristic features of the fluorescence spectrum associated with glucose metabolism. The incubation of albumin with glucose *in vitro* showed that there is a new fluorescence band, which is caused by the formation of cross-links giving fluorescence in the range 400–430 nm upon excitation at 320–350 nm. The fluorescent properties of this band are similar for different proteins (for example, for albumin and collagen), since one of the main glycation products that causes this fluorescence is pentosidine [14]. The refractive index (RI) is one of the most important optical characteristics of tissues and the knowledge of its dispersion and temperature dependences for various forms of hemoglobin is important for understanding the changes in the optical properties of blood and biological tissues [13, 22–25] Since the structure and composition of tissues and correspondingly their optical properties are changing in the course of pathology development, then several research groups have suggested the RI as a marker for differentiation of normal and pathological tissue, including experimental diabetes in animals [13, 22, 23].

In these studies, a comparative fluorescence analysis of hemoglobins was done for excitation wavelengths of 260, 270 and 280 nm. We also applied SERS to detect spectra from the dried drops of Hb and HbA1c. The RIs of two forms of hemoglobin were measured for 12 visible and NIR wavelengths (480–1550 nm) at temperature 25 °C and for wavelengths 546, 589, 644, 930 nm at temperatures from 23 to 43 °C. The RIs of hemoglobin solution for the control and diabetic groups were measured for a temperature range from 25 to 50 °C at 12 wavelengths.

2 Methods and Materials

The optical properties of solutions of glycated and non-glycated forms of hemoglobin were investigated by using a multimodal approach with three independent optical methods, which allows us to make a detailed comparison of optical properties and to reveal specific features of hemoglobins for their discrimination.

2.1 Samples

As samples of the study, solutions of pure Hb and HbA1c were taken. Lyophilized powder of human Hemoglobin (Hb) and hemolysate of glycated hemoglobin (HbA1c) (Sigma-Aldrich) were used. The dilution was performed with a physiological solution of 0.9% NaCl.

Refractometric measurements were also performed for hemoglobin obtained from the whole blood of healthy volunteers (control group) and patients with diabetes mellitus (diabetes group). Whole blood was drawn from the human vein. Immediately after collecting blood into a test tube, heparin was added to it. The sample of blood was taken at the State Health Care Organization “Saratov City Clinical Hospital No. 2 named after V. I. Razumovsky with the permission of the volunteers (patient information consent). The level of glucose in the blood samples was 14.5, 11.7, and 8.8 mmol/l according to the results of the biochemical analysis. To separate blood into fractions, centrifugation for 10 min at 2000 rpm and at room temperature was provided. This

resulted in the separation of blood plasma, leuko-platelet layer, and RBC suspension. To conduct hemolysis and preparation of hemoglobin solutions, RBC suspension was separated and placed in a vial for freezing in a freezer at a temperature of −15 °C for 24 h.

2.2 SERS Experiments

SERS spectra were obtained by CENTAUR U HR (NanoScanTechnology LTD, Russia and ZAO SolarLS, Republic of Belarus) unit equipped with a He-Ne laser (Coherent Inc., USA) with excitation ($\lambda = 632$ nm, radiation power of 37 mW on the sample with the spot of 3.2 μm in diameter). SERS spectra were recorded using a thermoelectrically cooled CCD with a temperature of –40 °C and 5 sec acquisition time set for detector matrix. A spectrometer with a holographic diffraction grating of 600 grates/mm was used. Wavenumber reproduction accuracy was 1 cm^{-1}. The spectral resolution was 1 cm^{-1}. Rayleigh scattering has been eliminated by the use of a notch filter. The CENTAUR U scientific has been calibrated with silicon at a static spectrum centered at 520 cm^{-1}. The sample holder has been mounted on a standard stage for an Olympus BX41 microscope. For SERS, substrates of island anodically-dissolved silver, deposited electrochemically on a polished copper base with an anodic dissolution depth of silver of 500 nm, were used. Solutions of hemoglobin and glycated hemoglobin at a concentration of 3 g/l each were deposited as drops on the substrate. Samples were dried in the open air. As a result, a ring with a higher thickness of the sample was formed at the edges of the dried drops. The diameter of the rings was not more than 3 mm. Measurements were carried out for 5 samples of each solution. KnowItAll Vibrational Spectroscopy Edition (Willey, UK) software was used for linear baseline correction and normalization of all original spectra and further analysis of peaks position and its intensity.

2.3 Fluorescence Spectroscopy

The studies were carried out using a fluorescence spectrometer Cary Eclipse (Varian, Belgium). Excitation wavelengths were selected as 260, 270, and 280 nm. The solutions for measurements were highly diluted to a concentration at which the optical density is 0.1 in the spectral region of excitation. The optical density was measured on a spectrometer UV-3600 (Shimadzu, Japan). The spectra of fluorescence excitation were processed by a Gaussian analysis in the program OriginLab Pro (USA).

2.4 Refractometric Measurement

The commercial Multi-wavelength refractometer Abbe DR-M2/1550 (Atago, Japan) was used to measure the RI of solutions of Hb and HbA1c at a concentration of 3 g/l each and hemoglobin solution from healthy donors and patients with diabetes mellitus. In the setup, the source of radiation was a high-power candescent lamp. To select the wavelength, we used narrow-band interference filters for (480 ± 2), (486 ± 2), (546 ± 2), (589 ± 2), (644 ± 2), (656 ± 2), (680 ± 5), (800 ± 5), (930 ± 6), (1100 ± 26), (1300 ± 25), and (1500 ± 25) nm. The measurement error introduced by the instrument amounts to ±0.0002. At the beginning of every measurement, the calibration of the instrument using the known tabulated value of the RI of distilled water was executed. The sample temperature during the measurements was kept by water circulation in the refractometer provided by a thermostat. The temperature was 25 °C when measuring the RI for 12 wavelengths. The RI of Hb and HbA1c was measured at the wavelengths of 546, 589, and 644 nm at temperatures from 23 °C to 43 °C. The RI of hemoglobin for the control and diabetic groups was measured for a temperature range of 25 °C to 50 °C at 12 wavelengths. The RI was calculated as averaged over 3 measurements for each of 3 samples of Hb, HbA1c, hemoglobin from the whole blood of a healthy donor and of a patient with diabetes mellitus.

3 Results and Discussion

SERS spectra of Hb and HbA1c are shown in Figs. 1, 2. Determination of the position of the peaks and normalization procedure were carried out using KnowItAll Vibrational Spectroscopy Edition (Willey, UK) software. First derivative for both Hb and HbA1c were taken to indicate difference in the spectral intensity.

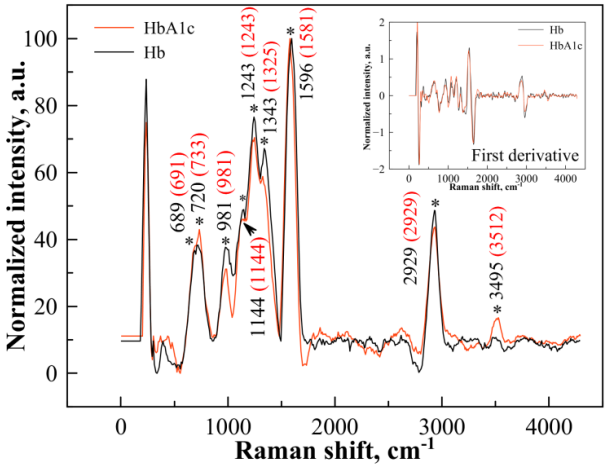


Fig. 1 Normalized SERS spectra acquired from dry drops of Hb (black line) and HbA1c (red line). Full spectral range (includes the first derivative of the spectra in the right top corner).

Differences in the spectra for Hb and HbA1c are observed mainly in the "fingerprint" region 0–1800 cm^{-1}. In this region, the position of the maxima of 10 peaks is established, the position of all peaks and their intensity have been described and analyzed to detect differences in the structure. The Hb and HbA1c spectra have been differentiated primarily based on peak shifts and secondary – on intensity.

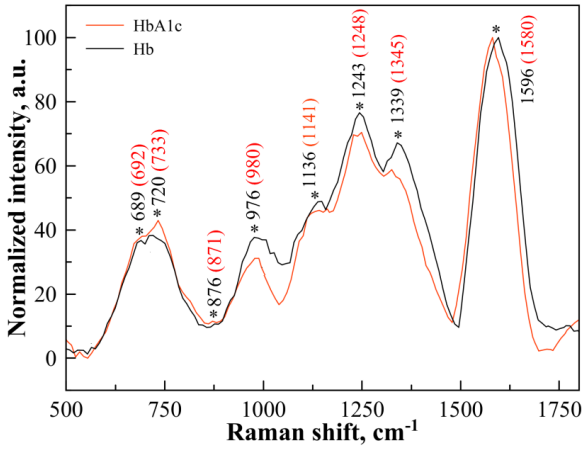


Fig. 2 Normalized SERS spectra acquired from dry drops of Hb (black line) and HbA1c (red line) for 500–1800 cm^{-1} "fingerprint" region.

Fig. 2 displays normalized SERS spectra of Hb and HbA1c. The band of FeO_2 at 1136 cm^{-1} [38] was observed for Hb and very low and shifted for HbA1c, confirming the fact of glycosylation of hemoglobin, which lowers oxygen-carrying capacity, that promotes hypoxia [26]. Barman et al. [12, 17] showed by using SERS that a high level of glucose in the blood not only influences protein function but also changes the structure of the heme. Importantly, the presence of subtle but distinct features in the difference spectra between Hb and HbA1c deposits highlights the sensitivity of the proposed approach to very small structural variations in the protein molecules. The variations in the two protein spectra can then be attributed to structural changes in hemoglobin molecules related to the binding of a glucose moiety [17, 27, 28]. For pyrrole rings scattering bands of δ(pyr deform)$_{sym}$, ν(pyr breathing), ν(pyr half-ring)$_{sym}$ at 689/692, 750/733, 1339/1345 have been detected, respectively. The fact of increased bands intensity (from 5.15% for δ(pyr deform)$_{sym}$ to 19.9% for ν(pyr breathing)) in HbA1c has been assigned to pyrrole ring polarization changes. Shifts in the pyrrole ring band can be also assigned to the chemical bond length of pyrrole molecules inside the pyrrole complex and its outer bonds. According to Ref. [38], pyrrole complex can change it orientation inside the molecule. Based on theoretical results in Ref. [39] hemoglobin exists in an ordered arrangement, such that the heme-porphyrin planes are preferentially orientated parallel to the RBCs' equatorial plane. The glycation of red blood cells can be precisely estimated using the electric/dielectric losses and polarization changes, described in detail in Ref. [40]. These factors lead to the spectral differences between the detected spectral shifts in pyrrole complex. Blue shift in tryptophan (Trp) scattering band with lowered intensity (of 7.86%) has been detected for Hb1A1c at 871 cm^{-1}. A slight blue shift in protein skeletal vibration and glutathione bands, substantially increased by 17.5% in the HbA1c case has been detected and this fact could be a possible marker of protein glycosylation [29]. No intensity changes have been detected in strong blue-shifted ν(C$_a$,C$_m$)$_{asym}$ band at 1596 cm^{-1} and 1580 cm^{-1} for Hb and HbA1c, respectively. The 16 cm^{-1} spectral shift can be explained by a change in the microenvironment of phenylalanine as a result of the transition of the molecule to the glycated form. The data for all well-defined positions of the maxima for Hb and HbA1c are given in Table 1.

Table 1 Well-defined Raman peak positions of Hb and HbA1c (cm^{-1}) and tentative assignments in "fingerprint" region*.

Hb	HbA1c	Vibrational modes	Reference	Δ_{int},%
689 vw	692 wsh	δ(pyr deform)$_{sym}$	[30]	5.15
750 vwsh	733 w	ν(pyr breathing), Trp	[11]	19.9
876 wv	871 wv	Trp	[16]	–7.86
976 mbr	980 mbr	p:Skeletal vibration, Glu	[11]	17.5
1136 wbr	1141 vwbr	δ(=C$_b$H$_2$)$_4$	[31]	5.33
1243 s	1248 s	δ(C$_m$H)	[27]	7.97
1339 m	1345 vwsh	ν(pyr half-ring)$_{sym}$, δ(C-C-H)	[16, 32]	12.52
1596 vs	1580 vs	ν(C$_a$,C$_m$)$_{asym}$, Phe	[11]	0
2933 s	2934 s	ν(CH$_3$)	[33]	10.03
3510 wbr	3512 mbr	H$_2$O	[30]	–54.85

*Abbreviations: w – weak; vw – very weak; m – medium; s – strong; vs – very strong; sh – shoulder; br – broad; δ – deformation vibration; ν – stretching vibration; Trp – tryptophan; Glu – glutathione; p – protein; Phe – phenilalnine;

$$\Delta_{\text{int}} = \frac{I_{Hb} - I_{HbA1c}}{I_{Hb}} \times 100.$$

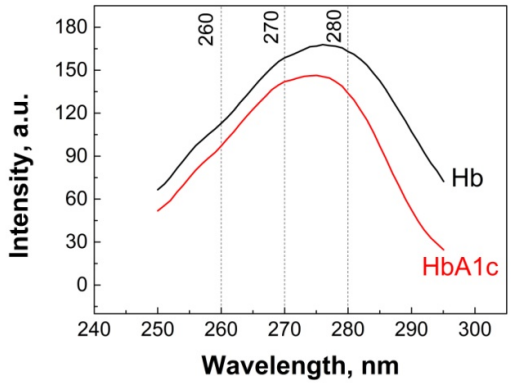


Fig. 3 Fluorescence excitation spectra of Hb and HbA1c.

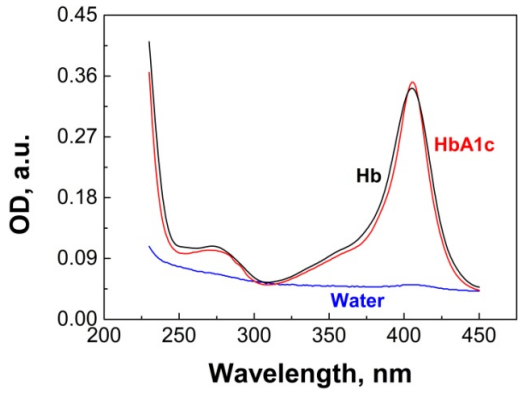


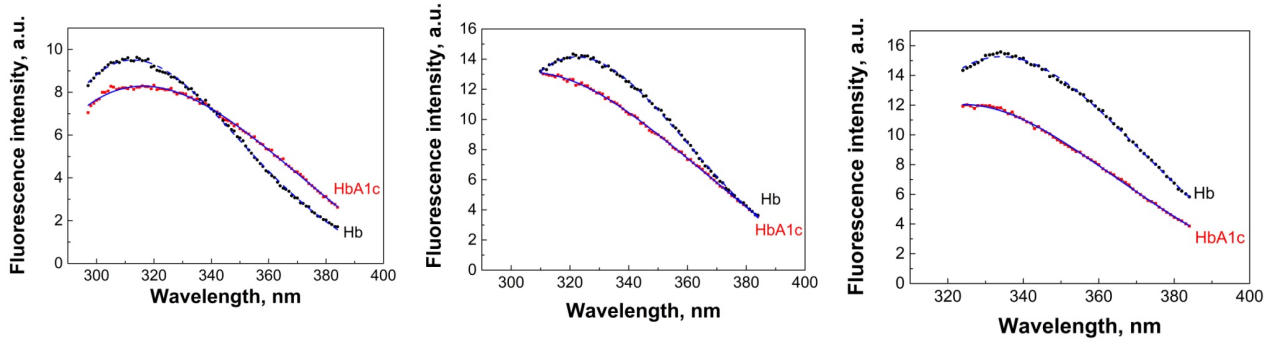
Fig. 4 Spectra of optical density of Hb, HbA1c and water.

The wavelengths of 260, 270, and 280 nm excitation of the fluorescence spectrum were selected for fluorescent analysis. The fluorescence excitation spectrum and spectrum of optical density of HbA1c and water for the selected region of excitation wavelengths are shown in Figs. 3, 4. These excitation wavelengths were chosen because of the published data where the peak of the hemoglobin fluorescence spectrum observed at 320 nm corresponds to the fluorescence of tryptophan that absorbs UV radiation with maxima at 220 nm and 280 nm and fluoresces in proteins at 328 ÷ 350 nm [20, 21]. Fig. 5 shows fluorescence spectra of solutions of Hb and HbA1c at excitation wavelengths of 260, 270, and 280 nm. The obtained spectral dependences were processed by Gaussian analysis in the program OriginLab Pro. The main parameters of fluorescence spectra of hemoglobin and glycated hemoglobin are given in Table 2.

According to the analysis of SERS spectra the vibrational activity of the constituent of the protein part of hemoglobin changes in the molecule HbA1c, while the detected fluorescence can be a fluorescence of the tryptophan and tyrosine parts of the molecule. The shift in the position of the peak in the short-wavelength region of the fluorescence spectrum of HbA1c for different excitation wavelengths can be explained by an increase in the contribution of tyrosine fluorescence. The change in the position of the fluorescence maximum of hemoglobin for different excitation wavelengths is explained by the change of the contribution of fluorescence of tryptophan and tyrosine. The amplification of the oscillations of tryptophan leads to quenching of tyrosine emission.

Analysis of SERS and fluorescence spectra showed that for the HbA1c molecule a partial quenching of tryptophan fluorescence occurs caused by increased vibrations of molecule nearby tryptophan, as a result, the contribution of tyrosine fluorescence increases. The relative change in fluorescence intensity of tryptophan and tyrosine leads to the formation of composite spectra, the position of the maxima of which is different from Hb.

For the first time in this paper, we have studied HbA1c dispersion and RI temperature increments in a wide spectral range using Abbe prism refractometry. Fig. 6a shows the dispersion of the RI of glycated and non-glycated hemoglobin solutions at 25 °C. The RI was measured for a temperature range of 23–43 °C for three selected wavelengths, 546, 589, 644, and 930 nm. The temperature dependence of the RI is shown in Fig. 6b.



(a) (b) (c)

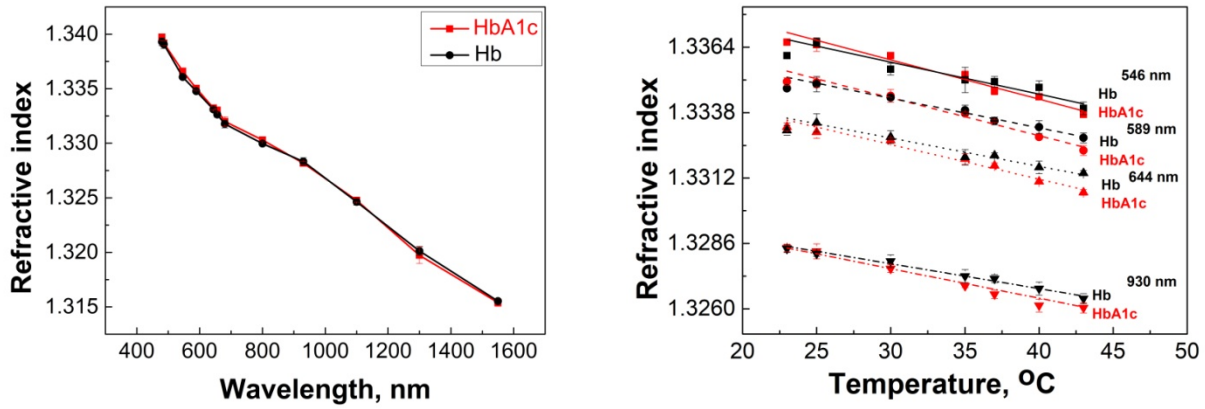
Fig. 5 Fluorescence spectra of Hb and HbA1c solutions with optical density of 0.1 at excitation wavelengths: (a) 260 nm; (b) 270 nm; (c) 280 nm (Hb– ■ (Black squares), HbA1c– ●(Red circles), Gaussian analysis – Blue lines).

Table 2 Parameters of fluorescence spectra of Hb and HbA1c: FWHM is the full width on half-maximum, FI is the fluorescence intensity (a.u.), and R^2 is the correlation coefficient.

Excitation wavelength	260 nm				270 nm				280 nm			
	λ, nm	FWHM	FI, a.u.	R^2	λ, nm	FWHM	FI, a.u.	R^2	λ, nm	FWHM	FI, a.u.	R^2
Hb	312	86	9.44	0.998	322	87	13.98	0.999	334	82	15.22	0.999
HbA1c	317	112	8.24	0.999	303	145	13.08	0.999	322	98	12.23	0.998
$\Delta_{HbA1c-Hb}$	5	26	0.35	–	–19	58	2.6	–	–12	16	–2.35	–

Table 3 Refractive index for $T = 0$ °C(n_0) and temperature increment (dn/dT) from the Eq. (1).

	546 nm		589 nm		644 nm		930 nm	
	n_0	$-dn/dT$, $\times10^{-4}$ °C^{-1}	n_0	$-dn/dT$, $\times10^{-4}$ °C^{-1}	n_0	$-dn/dT$, $\times10^{-4}$ °C^{-1}	n_0	$-dn/dT$, $\times10^{-4}$ °C^{-1}
Hb	1.3389 (±0.0005)	1.08 (±0.16)	1.3374 (±0.0003)	1.05 (±0.09)	1.3356 (±0.0004)	0.98 (±0.10)	1.3306 (±0.0003)	0.96 (±0.12)
HbA1c	1.3401 (±0.0005)	1.44 (±0.11)	1.3384 (±0.0003)	1.38 (±0.10)	1.3364 (±0.0003)	1.30 (±0.10)	1.3314 (±0.0003)	1.29 (±0.13)
$\Delta_{HbA1c-Hb}$	0.0012	0.36	0.0010	0.33	0.0008	0.32	0.0008	0.33



(a) (b)

Fig. 6 Dispersion measured at 25 °C (a) and temperature (b) dependencies of RI of Hb and HbA1c solutions at a concentration of 3 g/l.

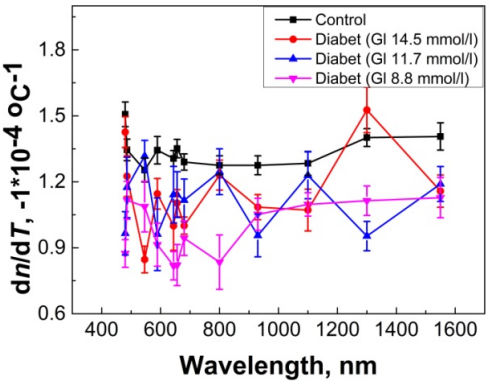
The temperature dependence for the interval 23–43 °C was approximated by a linear function:

$$n(T) = n_0 + (dn/dT)T, \quad (1)$$

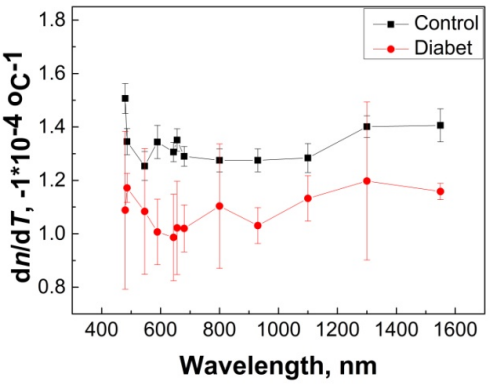
where n_0 is the RI for $T = 0$ °C; dn/dT is the RI derivative with respect to temperature or the temperature increment of the RI. The estimated values of n_0 and dn/dT for glycated and non-glycated hemoglobin forms are given in Table 3.

Based on the results obtained, we found an increase of the modulus of temperature increment for the glycated form of hemoglobin by an average of $(0.34 \pm 0.02)\times10^{-4}$ °C^{-1} for the wavelengths 546, 589, 644, and 930 nm. The total derivative of the RI with respect to temperature is related to the effect of thermal expansion and the temperature dependence of the molecular polarizability [34, 35]. In connection with this, the differences obtained in this study for Hb and HbA1c can be explained by their different molecular structure. The relationship between the polarizability of a molecule and the RI of a medium composed of these molecules is well described [34, 35]. The additivity rule is valid for molecular complexes consisting of molecules with different polarizabilities. In this case, the total polarizability is considered equal to the sum of the polarizability of each of the molecules. Thus, the molecular complex of hemoglobin with glucose has a larger molecular polarizability and RI depends on the content of charged amino acids in the molecule. The

dependence of the RI of dry erythrocytes from diabetic patients on pH (pH = 2–13) and, consequently, on the charge of the protein R-group was shown by Mazarevica et al. by using polarization-sensitive interference microscopy for the wavelength 550 nm [36].



(a)



(b)

Fig. 7 The wavelength dependence of RI temperature increment: (a) for healthy volunteers and diabetic patients with different levels of free glucose; (b) mean values for healthy (control) and diabetic groups.

We also studied the temperature dependence of the RI of hemoglobin obtained from whole blood of healthy people (control group) and patients with diabetes mellitus (diabetic group). In order to avoid influence of variations of hemoglobin concentration from sample to sample, the normalization of RI values for different patients was carried out by using this formula:

$$n_{\text{norm}} = \frac{n_\lambda}{n_{\lambda,\max}}, \qquad (2)$$

Figs. 7a and 7b show that for the diabetic group the temperature increment is lower than for the healthy (control) group. It should be noted that in these samples a hemoglobin solution consisting of various hemoglobin fractions was studied, the concentration of which considerably exceeds the physiological concentration of glycated hemoglobin. However, the graphs show that for the diabetic group the temperature increment is lower than for the healthy (control) group which is contradictory to data obtained for the temperature increment of glycated and non-glycated hemoglobin samples prepared from hemolysate of HbA1c and lyophilized powder of human Hb, respectively. Evidently, this is due to differences in the studied samples. Dry for Hb / HbA1c measurements and Hemoglobin extracted from the whole blood of healthy and diabetic subjects may contain additional molecular components that may have different temperature increments. The high level of free glucose in the blood (8.8–14.5 mmol/l) also may have an impact on the value of increment. In fact, statistically significant differences of measured RI temperature increments of hemoglobin from healthy and diabetic subjects on the wavelengths 589, 644, 656, 680, 930, 1100, and 1500 nm are found.

Thus, optical methods used in the work demonstrate the possibility of detection of small amounts of HbA1c on the background of Hb in their mixtures directly without any chemical reaction. High sensitivity has the refractometric method applied for the first time to measure RI temperature increments for different wavelengths.

4 Conclusion

Analysis of three different optical methods revealed the presence of characteristic features allowing for discrimination glycated HbA1c and normal Hb hemoglobins. SERS demonstrated well detectable differences of Raman bands and their intensities mainly in the “fingerprint” region of 500–1800 cm^{-1}. Revealed features can be used as HbA1c markers in hemoglobin mixtures. Fluorescence spectroscopy showed the presence of characteristic distinctive features for glycated hemoglobin at excitation on the wavelength of 270 nm. The average increase in the refractive index temperature increment modulus of HbA1c in comparison to Hb in the visible and NIR spectral regions is of $(0.34 \pm 0.02)\times10^{-4}\,°C^{-1}$.

The data obtained in this work confirm and supplement those that are available in the literature, and can also serve as a basis for further study of the optical properties of glycated hemoglobin and other glycated proteins. Data received are important for the development of optical diagnostic and therapeutic methods, in particular for *in vivo* fluorescent and photoacoustic cytometry of melanoma cells in the bloodstream of diabetic patients.

Disclosures

The authors have no relevant financial interests in this article and no potential conflicts of interest to disclose.

Acknowledgements

I. G. Samusev and A. Y. Zyubin was supported by state contract of the RF Ministry of Science and Higher Education of the Russian Federation (FZWM-2020-0003).

E. N. Lazareva acknowledges financial support of the RFBR grant 20-32-90058 for fluorescence and refraction measurements.

A. B. Bucharskaya and V. V. Tuchin acknowledge financial support of the grant under the Decree of the Government of the Russian Federation No. 220 of 09 April 2010 (Agreement No. 075-15-2021-615 of 04 June 2021).

References

1. M. Smiga, J. W. Smalley, P. Ślęzak, J. L. Brown, K. Siemińska, R. E. Jenkins, E. A. Yates, and T. Olczak, "Glycation of Host Proteins Increases Pathogenic Potential of Porphyromonas gingivalis," International Journal of Molecular Sciences 22(12), 12084 (2021).
2. S. Yazdanpanah, M. Rabiee, M. Tahriri, M. Abdolrahim, A. Rajab, H. E. Jazayeri, and L. Tayebi, "Evaluation of glycated albumin (GA) and GA/HbA1c ratio for diagnosis of diabetes and glycemic control: A comprehensive review," Journal Critical Reviews in Clinical Laboratory Sciences 54(4), 3 (2017).
3. E. Selvin, M. W. Steffes, H. Zhu, K. Matsushita, L. Wagenknecht, J. Pankow, J. Coresh, and F. L. Brancati, "Glycated hemoglobin, diabetes, and cardiovascular risk in nondiabetic adults," New England Journal of Medicine 362(9), 800–811 (2010).
4. T. Pan, M. Li, J. Chen, and H. Xue, "Quantification of glycated hemoglobin indicator HbA1c through near-infrared spectroscopy," Journal of Innovative Optical Health Sciences 7(4), 1350060 (2014).
5. P. Dong, H. Lin, K. Huang, and J. Cheng, "Label-free quantitation of glycated hemoglobin in single red blood cells by transient absorption microscopy and phasor analysis," Science Advances 5(5), eaav0561 (2019).
6. Executive Summary: Standards of Medical Care in Diabetes, Diabetes Care 33 (Supplement 1), S4-S10 (2010).
7. V. V. Tuchin, A. Tárnok, and V. P. Zharov, "In vivo flow cytometry: A horizon of opportunities," Cytometry Part A 79(10), 737–745 (2011).
8. D. A. Nedosekin, M. A. Juratli, M. Sarimollaoglu, C. L. Moore, N. J. Rusch, M. S. Smeltzer, V. P. Zharov, and E. I. Galanzha, "Photoacoustic and photothermal detection of circulating tumor cells, bacteria and nanoparticles in cerebrospinal fluid in vivo and ex vivo," Journal of Biophotonics 6(6–7), 523–533 (2013).
9. D. A. Nedosekin, M. Sarimollaoglu, J.-H. Ye, E. I. Galanzha, and V. P. Zharov, "In vivo ultra-fast photoacoustic flow cytometry of circulating human melanoma cells using near-infrared high-pulse rate lasers," Cytometry Part A 79(10), 825–833 (2011).
10. J. Q. Lin, R. Chen, S. Feng, J. Pan, Y. Li, G. Chen, M. Cheng, Z. Huang, Y. Yu, and H. Zeng, "A novel blood plasma analysis technique combining membrane electrophoresis with silver nanoparticle based SERS spectroscopy for potential applications in non-invasive cancer detection," Nanomedicine: Nanotechnology, Biology and Medicine 7(5), 655–663 (2011).
11. J. Lin, J. Lin, Z. Huang, P. Lu, J. Wang, X. Wang, and R. Chen, "Raman spectroscopy of human hemoglobin for diabetes detection," Journal of Innovative Optical Health Sciences 7(1),1350051 (2014).
12. I. Barman, N. C. Dingari, J. W. Kang, G. L. Horowitz, R. R. Dasari, and M. S. Feld, "Raman spectroscopy-based sensitive and specific detection of glycated hemoglobin," Analytical Chemistry 84(5), 2474−2482 (2012).
13. O. S. Zhernovaya, V. V. Tuchin, and I. V. Meglinski, "Monitoring of blood proteins glycation by refractive index and spectral measurements," Laser Physics Letters 5(6), 460–464 (2008).
14. E. Shirshin, O. P. Cherkasova, T. Tikhonova, E. Berlovskaya, A. V. Priezzhev, and V. Fadeev, "Native fluorescence spectroscopy of blood plasma of rats with experimental diabetes: identifying fingerprints of glucose-related metabolic pathways," Journal of Biomedical Optics 20(5), 051033 (2015)
15. S. Y. Feng, R. Chen, J. Lin, J. Pan, G. Chen, Y. Li, M. Cheng, Z. Huang, J. Chen, and H. Zeng, "Nasopharyngeal cancer detection based on blood plasma surface-enhanced Raman spectroscopy and multivariate analysis," Biosensors and Bioelectronics 25(11), 2414–2419 (2010).
16. H. W. Han, X. L. Yan, R. X. Dong, G. Ban, and K. Li, "Analysis of serum from type II diabetes mellitus and diabetic complication using surface-enhanced Raman spectra (SERS)," Applied Physics B 94(4), 667– 672 (2009).
17. I. Barman, N. C. Dingari, J. W. Kang, G. L. Horowitz, R. R. Dasari, and M. S. Feld, "Raman spectroscopy based sensitive and specific detection of glycated hemoglobin," Analytical Chemistry 84(5), 2474–2482 (2012).
18. M. S. Kiran, T. Itoh, K.-I. Yoshida, N. Kawashima, V. Biju, and M. Ishikawa, "Selective Detection of HbA1c Using Surface Enhanced Resonance Raman Spectroscopy," Analytical Chemistry 82(2), 1342−1348 (2010).
19. M. Sackmann, S. Bom, T. Balster, and A. Materny, "Nanostructured gold surfaces as reproducible substrates for surface-enhanced Raman spectroscopy," Journal of Raman Spectroscopy 38(3), 277−282 (2007).
20. J. T. Liu, L.-Y. Chen, M.-C. Shih, Y. Chang, and W.-Y. Chen, "The investigation of recognition interaction between phenyl boronate monolayer and glycated hemoglobin using surface plasmon resonance," Analytical Biochemistry 375(1), 90–96 (2008).
21. J. Li, K.-W. Chang, C.-H. Wang, C.-H. Yang, S.-C. Shiesh, and G.-B. Lee, "On-chip, aptamer-based sandwich assay for detection of glycated hemoglobins via magnetic beads," Biosensors and Bioelectronics 79, 887–893 (2016).

22. P. Giannios, S. Koutsoumpos, K. G. Toutouzas, M. Matiatou, G. C. Zografos, and K. Moutzouris, "Complex refractive index of normal and malignant human colorectal tissue in the visible and near-infrared," Journal of Biophotonics 10(2), 303–310 (2017).
23. S. Carvalho, N. Gueiral, E. Nogueira, R. Henrique, L. Oliveira, and V. V. Tuchin, "Wavelength dependence of the refractive index of human colorectal tissues: comparison between healthy mucosa and cancer," Journal of Biomedical Photonics and Engineering 2(4), 040307 (2016).
24. K. Zirk, H. Poetzschke, "On the suitability of refractometry for the analysis of glucose in blood-derived fluids," Medical Engineering & Physics 26(6), 473–481 (2004).
25. K. Zirk, H. Poetzschke, "A refractometry-based glucose analysis of body fluids," Medical Engineering & Physics 29(4), 449–458 (2007).
26. S. I. Sherwani, H. A. Khan, A. Ekhzaimy, A. Masood, and M. K. Sakharkar,"Significance of HbA1c test in diagnosis and prognosis of diabetic patients," Biomarker Insights 11, BMI-S38440 (2016).
27. B. R. Wood, P. Caspers, G. J. Puppels, S. Pandiancherri, and D. McNaughton,"Resonance Raman spectroscopy of red blood cells using near-infrared laser excitation," Analytical and Bioanalytical Chemistry 387(5), 1691–1703 (2007).
28. R. Ghosh Moulick, J. Bhattacharya, S. Roy, S. Basak, and A. K. Dasgupta, "Compensatory secondary structure alterations in protein glycation," Biochimica et Biophysica Acta (BBA) – Proteins and Proteomics 1774, 233−242 (2007).
29. D. P. Cowcher, T. Deckert-Gaudig, V. L. Brewster, L. Ashton, V. Deckert, and R. Goodacr, "Detection of protein glycosylation using tip-enhanced Raman scattering," Analytical Chemistry 88(4), 2105–2112 (2016).
30. Q. Sun, "The Raman OH stretching bands of liquid water," Vibrational Spectroscopy 51(2), 213–217 (2009).
31. G. Rusciano, A. C. De Luca, G. Pesce, and A. Sasso, "Raman tweezers as a diagnostic tool of hemoglobin-related blood disorders," Sensors 8(12), 7818–7832 (2008).
32. C. R. Yonzon, C. L. Haynes, X. Zhang, J. T. Walsh, and R. P. Van Duyne, "A glucose biosensor based on surface-enhanced Raman scattering: improved partition layer, temporal stability, reversibility, and resistance to serum protein interference," Analytical Chemistry 76(1), 78–85 (2004).
33. J. Lin, Y. Zeng, J. Lin, J. Wang, L. Li, Z. Huang, B. Li, H. Zeng, and R. Chen, "Erythrocyte membrane analysis for type II diabetes detection using Raman spectroscopy in high-wavenumber region," Applied Physics Letters 104(10), 104102 (2014).
34. A. I. Erokhin, N. V. Morachevskii, and F. S. Faizullov, "Temperature dependence of the refractive index in condensed media," Journal of Experimental and Theoretical Physics 74, 1336–1341 (1978).
35. M. V. Volkenshtein, Molecular Optics, Gosteskhizdat, Moscow (1951) [in Russian].
36. G. Mazarevica, T. Freivalds, and A. Jurka, "Properties of erythrocyte light refraction in diabetic patients," Journal of Biomedical Optics 7(2), 244–247 (2002).
37. T. K. Das, M. Couture, Y. Ouellet, M. Guertin, and D. L. Rousseau, "Simultaneous observation of the O-O and Fe-O_2 stretching modes in oxyhemoglobins," Proceedings of the National Academy of Sciences 98(2), 479–484 (2001).
38. C. G. Atkins, K. Buckley, M. W. Blades, and R. F. B. Turner, "Raman spectroscopy of blood and blood components," Applied Spectroscopy 71(5), 767–793 (2017).
39. S. Ahlawat, A. Chowdhury, N. Kumar, A. Uppal, R. S. Verma, and P. K. Gupta, "Polarized Raman Spectroscopic Investigations on Hemoglobin Ordering in Red Blood Cells," Journal of Biomedical Optics 19(8), 87002 (2014).
40. S. Abdalla, F. Farsaci, E. Tellone, W. Shirbeeny, A. M. Hassan, F. Bahabri, and S. Kandil, "Hemoglobin glycation increases the electric charges on red blood cells: Effects of dielectric polarization," Materials Chemistry and Physics 276, 125348 (2022).

Porous Silicon Nanoparticles with Rare Earth as Potential Contrast Agents for MRI and Luminescent Probes for Bioimaging

Anastasiya D. Mironova[1*], Yulia V. Kargina[1,2], Olga S. Pavlova[2,3], Alexander M. Perepukhov[4], Igor O. Sobina[2], and Victor Yu. Timoshenko[1,2]

[1] Phys-Bio Institute, National Research Nuclear University "MEPhI", 31 Kashirskoe shosse, Moscow 115409, Russia
[2] Faculty of Physics, Lomonosov Moscow State University, 1 Leninskie Gory, Moscow 119991, Russia
[3] Faculty of Fundamental Medicine, Lomonosov Moscow State University, 1 Leninskie Gory, Moscow 119991, Russia
[4] Institute of Physics and Technology, 9 Institutskiy per., Dolgoprudny 141700, Moscow Region, Russia

*** e-mail:** navonorim@mail.ru

Abstract. Nanoparticles of porous silicon with incorporated europium and gadolinium ions were prepared by using mechanical grinding of electrochemically grown mesoporous silicon films followed with impregnation with rare earth ions from aqueous solutions. The photoluminescence spectroscopy of europium doped porous silicon nanoparticles allowed us to reveal narrow lines associated with the $^5D_0 \rightarrow {}^7F_4$ transitions in Eu^{3+} ions. Measurements of the proton relaxation in aqueous suspensions of nanoparticles with embedded Gd^{3+} ions showed an effect of the shortening of both the longitudinal and transverse relaxation times. Potential applications of rare earth doped porous silicon nanoparticles as contrast agents in MRI and fluorescent labels in bioimaging are discussed.
© 2022 Journal of Biomedical Photonics & Engineering.

Keywords: nanoparticles; aqueous suspensions; proton relaxation; magnetic resonance imaging; contrast agent.

Paper #3477 received 19 Feb 2022; revised manuscript received 4 Apr 2022; accepted for publication 1 May 2022; published online 18 May 2022. doi: 10.18287/JBPE22.08.020304.

1 Introduction

Magnetic resonance imaging (MRI) is widely used in medical practice because this diagnostic method is safe and has a high spatial resolution [1]. Molecular substances called contrast agents (CAs) can significantly enhance the MRI contrast [2, 3]. Novel CAs based on nanoparticles (NPs) are being studied and developed [4]. Most clinically approved types of CAs consist of ions of gadolinium (Gd) [5–7] and iron (Fe) [8, 9]. Recently new types of CAs based on silicon (Si) NPs have been proposed [10, 11]. It was shown that CA properties of Si NPs could be significantly improved after incorporation of Fe^{3+} [12]. However, Gd-based substances are one of the most common CAs for clinical diagnostic purposes. They have a high relaxivity and increase the signal intensity due to a decrease in the longitudinal relaxation that is explained by the interaction of proton spins of water molecules with electron spins of rare earth ions [3, 13–15]. The disadvantage is the toxicity of free Gd^{3+} ions, which can cause allergic reactions in some patients. To reduce the toxic effect of free Gd^{3+} ions, it is proposed to bind them with biocompatible Si NPs and reduce the concentration of ions in the CA. It is important that the CA remains effective. Besides Gd^{3+}, trivalent ions Eu^{3+} are considered as potential labels in biomedical diagnostics [16]. The aim of our work is to study the effect of incorporated Gd^{3+} and Eu^{3+} ions in porous Si NPs on the proton relaxation in aqueous solutions as well the photoluminescence property rare earth doped MPSi NPs as possible CAs for MRI and probes for fluorescent bioimaging.

2 Materials and Methods

Aqueous suspensions of mesoporous Si (MPSi) NPs were prepared by electrochemical etching of crystalline Si (c-Si) wafers followed by mechanical grinding of the formed mesoporous films in water by using a planetary mill [10]. To obtain a uniform distribution of MPSi NPs

in water, all samples were exposed to ultrasound for 30 min. Then, suspensions of MPSi NPs with concentration about 10 mg/mL were mixed with aqueous solutions of lanthanide chlorides ($EuCl_3$ and $GdCl_3$) at different concentrations of the latter varied from 10 to 50 mg/mL. The prepared mixtures were stored for 30 min followed with centrifugation and cleaning by deionized water two times to remove unbound lanthanide ions. Then the samples were diluted to obtain aqueous suspensions of MPSi:Gd and MPSi:Eu NPs with concentration of the order of 1 mg/mL.

The hydrodynamic diameter and surface charge (zeta-potential) of the MPSi NPs were estimated by using a methods of the dynamic light scattering (DLS) with a ZetasizerNano Malvern DLS spectrometer (Malvern Instruments, United Kingdom). A part of the prepared aqueous suspensions was dried at room temperature in air to analyze their chemical composition by means of the X-ray fluorescence (XRF) spectroscopy using a Renom apparatus (Expert Center Ltd., Russia). Photoluminescence (PL) spectra of MPSi NPs and those with Eu^{3+} ions under excitation with a semiconductor laser at 465 nm were measured by using a grating monochromator equipped with a CCD unit (Mightex, Canada). To measure the proton relaxation times in aqueous suspensions of MPSi NPs we used a Bruker Minispec NMR relaxometer (Bruker, Germany) with a constant magnetic field strength of about 0.5 T. The relaxation times were measured for 800 μL of aqueous suspensions of NPs in glass ampoules placed in a thermostat at 40 °C.

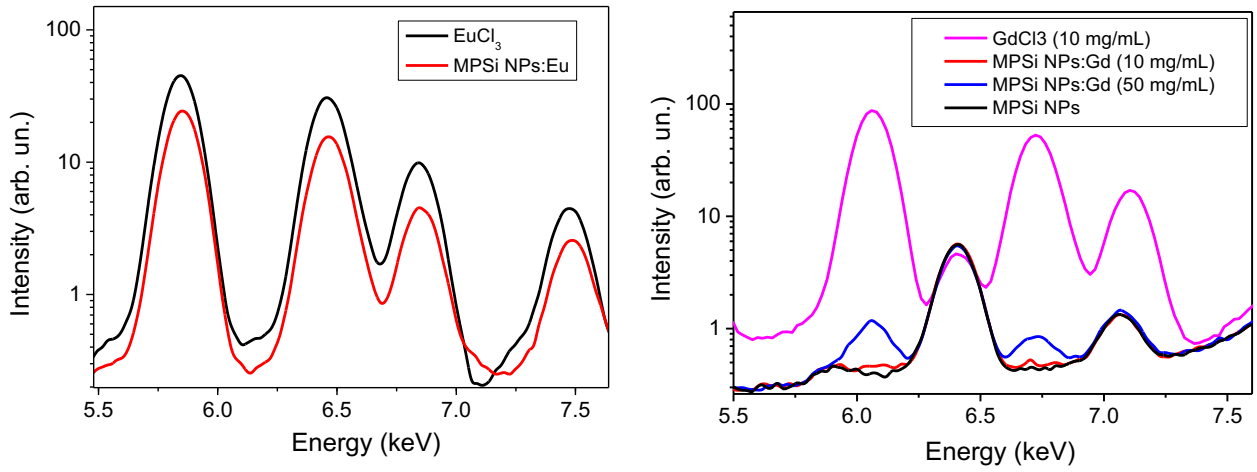
3 Results and Discussion

DLS measurements reveal that prepared MPSi NPs are characterized by hydrodynamic diameter and zeta-potential of about 560 nm and –6 mV, respectively. The negative value of the latter indicates the predominant role of hydroxyl groups on the surface of MPSi NPs [10]. The initial negative charge of NPs can obviously promote the electrostatic binding between the NP's surface and positively charged lanthanide ions, i.e. Gd^{3+} and Eu^{3+} in aqueous solutions.

Fig. 1 shows typical XRF spectra of MPSi NPs with incorporated rare earth and reference samples of dried lanthanide chlorides and initial MPSi NPs. The characteristic X-ray emission lines of the L-series in Europium at 5.82-5.85, 6.46, 6.84 and 7.48 keV [17] are detected for $EuCl_3$ and MPSi:Eu NPs (see Fig. 1a). The characteristic L-shell lines of the Gadolinium at 6.03–6.06, 6.71, 7.10, and 7.79 keV [17] are also detected in MPSi:Gd NPs prepared at the initial rare earth concentration about 10 mg/mL (see Fig 2b). By comparing with the XRF line intensities the europium concentration in MPSi:Eu are estimated to be about 48.7 at.% that indicates a high efficiency of the incorporation of Eu^{3+} ions into MPSi NPs. This fact can be explained by high internal surface area and negative surface charge of the latter [18]. The Gd content is about 0.09 and 0.33 at.% in MPSi NPs samples prepared at the $GdCl_3$ concentration of 10 mg/mL and 50 mg/mL, respectively. The smaller relative content of rare earth in MPSi:Gd NPs in comparison with that in MPSi:Eu ones can be related to different efficiency of the incorporation into oxidized internal surface of MPSi. Table 1 presents XRF data on the rare earth concentration in the samples under study.

Table 1 Rare earth content in MPSi NPs according to XRF data.

Sample	Rare earth content, at.%
MPSi:Eu (46mg/mL)	48.70
MPSi:Gd (50 mg/mL)	0.33
MPSi:Gd (10 mg/mL)	0.09



(a) (b)

Fig. 1 XRF spectra of the following samples: (a) $EuCl_3$ (46 mg/mL) and MPSi NPs with Eu^{3+} ions incorporated from aqueous solution with the same rare earth concentration; (b) $GdCl_3$ (10 mg/mL), MPSi NPs with Gd^{3+} ions incorporated from aqueous solutions at different concentrations and pure MPSi NPs.

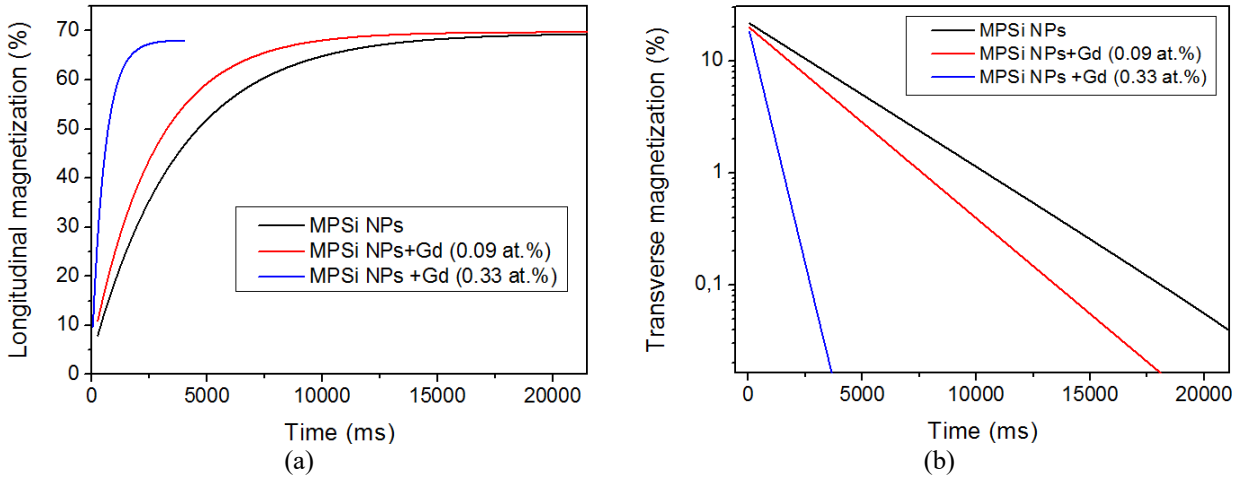


Fig. 2 Transients of the longitudinal (a) and transverse (b) components of the proton magnetization for aqueous suspensions of MPSi NPs and those with incorporated Gd^{3+} ions with different concentration.

Fig. 2 shows transients of the longitudinal and transverse components of the proton magnetization for suspensions of MPSi:Gd NPs. While pure MPSi NPs do not significantly affect the proton relaxation, Gd^{3+} ions introduced into the NPs lead to a shortening of both the longitudinal and transverse relaxation times. Table 2 summarizes the times of longitudinal and transverse proton relaxation for pure MPSi NPs and those with incorporated rare earth ions. It is seen that MPSi:Eu NPs are not effective CA for MRI because of the well-known low relaxivity efficiency of Eu^{3+} ions, in contrast to MPSi NPs with Gd^{3+} ions, which decrease the relaxation times by 3 orders of magnitude.

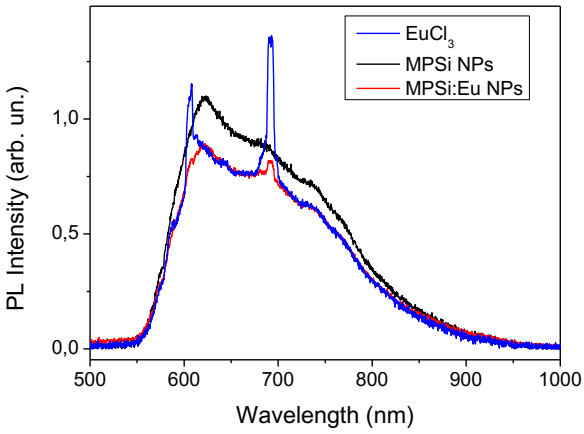


Fig. 3 PL spectra of aqueous solution of $EuCl_3$, suspensions of MPSi and MPSi:Eu NPs.

Fig. 3 shows PL spectra of MPSi:Eu NPs, $EuCl_3$, and pure MPSi NPs. The spectra of $EuCl_3$ and MPSi NPs with incorporated Eu^{3+} ions exhibit characteristic narrow lines associated with the $^5D_0 \rightarrow {}^7F_4$ transition in Eu^{3+} [16, 19]. The broad PL band in the region from 550 nm to 900 nm can be related to the radiative emission processes in the hydroxide layer of MPSi NPs [18] as well as in optically excited Eu^{2+}ions [19]. It is interesting to note that in our experiments the Eu^{3+}PL is efficiently excited by the green-blue light with wavelength of 465 nm, which corresponds to relatively weak absorption due to the $^7F_0 \rightarrow {}^5D_2$ transition in Eu^{3+}[19]. The possibility to excite MPSi:Eu NPs by visible light seems to be useful for bioimaging application [16].

Table 2 Data on the longitudinal (T_1) and transverse (T_2) relaxation times for aqueous suspensions of MPSi NPs without and with rare earth incorporation as well for the corresponding lanthanide salts and water for comparison.

Sample	**T_1 (ms)**	**T_2 (ms)**
Water	4360 ± 10	3500 ± 10
MPSi, 1 mg/mL	3784 ± 10	3452 ± 10
$EuCl_3$, 46 mg/mL	2297 ± 10	2012 ± 10
$GdCl_3$, 1 mg/mL	3.2 ± 0.6	2.77 ± 0.06
MPSi:Gd (0.09 at. %), 1 mg/mL	2769 ± 10	2540 ± 10
MPSi:Gd (0.33 at. %), 1 mg/mL	565 ± 5	514 ± 5

4 Conclusions

Aqueous suspensions of mesoporous Si NPs with incorporated Eu^{3+} and Gd^{3+} ions are prepared by using mechanical grinding of the electrochemically grown mesoporous silicon films followed with impregnation by the rare earth in concentrated aqueous solutions of the corresponding lanthanide chlorides. It is established that Gd^{3+} ions incorporated into MPSi NPs even at low concentration about 0.33 at.% can significantly decrease both the longitudinal and transverse times of the proton relaxation in water molecules in aqueous media. This observation opens new possibilities for Gd-doped MPSi NPs as potential CA in biomedical MRI diagnostics. The good degree of binding and characteristic PL emission in the visible spectral range of Eu^{3+} ions are found for MPSi

NPs impregnated with rare earth in $EuCl_3$ solutions. This optical property can be of interest for applications of Eu-doped MPSi NPs, for example, as fluorescent probes in bioimaging.

Disclosures

The authors have no relevant financial interests in this article and no potential conflicts of interest to disclose.

References

1. J. C. Weinreb, H. C. Redman, "Musculoskeletal System," Chapter 12 in Magnetic Resonance Imaging of the Body: Advanced Exercises in Diagnostic Radiology Series, J. C. Weinreb, H. C. Redman, Saunders, Philadelphia, 214–259 (1987).
2. S. Aime, A. Barge, C. Cabella, S. G. Crich, and E. Gianolio, "Targeting cells with MR imaging probes based on paramagnetic Gd(III) chelates," Current Pharmaceutical Biotechnology 5(6), 509–518 (2004).
3. A. Y. Louie, M. M. Hüber, E. T. Ahrens, U. Rothbächer, R. Moats, R. E. Jacobs, S. E. Fraser, and T. J. Meade, "In vivo visualization of gene expression using magnetic resonance imaging," Nature Biotechnology 18, 321–325 (2000).
4. O. Salata, "Applications of nanoparticles in biology and medicine", Journal of Nanobiotechnology 2, 3 (2004).
5. P.-J. Debouttière, S. Roux, F. Vocanson, C. Billotey, O. Beuf, A. Favre-Réguillon, Y. Lin, S. Pellet-Rostaing, R. Lamartine, P. Perriat, and O. Tillement, "Design of Gold Nanoparticles for Magnetic Resonance Imaging," Advanced Functional Materials 16(18), 2330–2339 (2006).
6. F. Lux, V. L. Tran, E. Thomas et al., "AGuIX® from bench to bedside—Transfer of an ultrasmall theranostic gadolinium-based nanoparticle to clinical medicine," The British Journal of Radiology 92(1093), 20180365 (2018).
7. J. Morlieras, S. Dufort, L. Sancey, C. Truillet, A. Mignot, F. Rossetti, M. Dentamaro, S. Laurent, L. V. Elst, R. N. Muller, R. Antoine, P. Dugourd, S. Roux, P. Perriat, F. Lux, J.-L. Coll, and O. Tillement, "Functionalization of small rigid platforms with cyclic RGD peptides for targeting tumors overexpressing αvβ3 integrins," Bioconjugate Chemistry 24(9), 1584–1597 (2013).
8. K. Ishiyama, S. Motoyama, N. Tomura, R. Sashi, H. Imano, J.-I. Ogawa, K. Narita, and J. Watarai, "Visualization of lymphatic basin from the tumor using magnetic resonance lymphography with superparamagnetic iron oxide in patients with thoracic esophageal cancer," Journal of Computer Assisted Tomography 30(2), 270–275 (2006).
9. A. Tanimoto, S. Kuribayashi, "Application of superparamagnetic iron oxide to imaging of hepatocellular carcinoma," European Journal of Radiology 58(2), 200–216 (2006).
10. Y. V. Kargina, M. B. Gongalsky, A. M. Perepukhov, A. A. Gippius, A. A. Minnekhanov, E. A. Zvereva, A. V. Maximychev, and V. Yu. Timoshenko, "Investigation of proton spin relaxation in water with dispersed silicon nanoparticles for potential magnetic resonance imaging applications," Journal of Applied Physics 123(10), 104302 (2018).
11. Y. V. Kargina, A. M. Perepukhov, A. Yu. Kharin, E. A. Zvereva, A. V. Koshelev, S. V. Zinovyev, A. V. Maximychev, A. F. Alykova, N. V. Sharonova, V. P. Zubov, M. V. Gulyaev, Y. A. Pirogov, A. N. Vasiliev, A. A. Ischenko, and V. Yu. Timoshenko, "Silicon nanoparticles prepared by plasma-assisted ablative synthesis: physical properties and potential biomedical applications," Physica Status Solidi (A) 216(14), 1800897 (2019).
12. Y. V. Kargina, S. V. Zinovyev, A. M. Perepukhov, E. V. Suslova, A. A. Ischenko, and V. Yu. Timoshenko, "Silicon nanoparticles with iron impurities for multifunctional applications," Functional Materials Letters 13(4), 2040007 (2020).
13. K. N. Raymond, V. C. Pierre, "Next generation, high relaxivity gadolinium MRI agents," Bioconjugate Chemistry 16(1), 3–8 (2005).
14. Z. Wang, F. Carniato, Y. Xie, Y. Huang, Y. Li, S. He, N. Zang, J. D. Rinehart, M. Botta, and N. C. Gianneschi, "High relaxivity gadolinium-polydopamine nanoparticles," Small 13(43), 1701830 (2017).
15. M. Engström, A. Klasson, H. Pedersen, C. Vahlberg, P.-O. Käll, and K. Uvdal, "High proton relaxivity for gadolinium oxide nanoparticles," Magnetic Resonance Materials in Physics, Biology and Medicine 19(4), 180–186 (2006).
16. M. Donmez, H. A. Oktem, and M. D. Yilmaz, "Ratiometric fluorescence detection of an anthrax biomarker with Eu^{3+}-chelated chitosan biopolymers," Carbohydrate Polymers 180, 226–230 (2018).
17. J. A. Bearden, "X-Ray Wavelengths," Reviews of Modern Physics 39(1), 78–124 (1967).
18. A. S. Eremina, Y. Kargina, A. Y. Kharin, D. I. Petukhov, and V. Y. Timoshenko, "Mesoporous silicon nanoparticles covered with PEG molecules by mechanical grinding in aqueous suspensions," Microporous and Mesoporous Materials 331, 111641 (2022).
19. I. N. Ogorodnikov, V. A. Pustovarov, "Linear optical, luminescence and electronic properties of the La2Be2O5 laser crystals doped with Ce3+ or Eu3+," Journal of Luminescence 162, 50–57 (2015).

Study of Laser-Induced Microdeformations of the Cornea Using Phase-Sensitive Optical Coherent Elastography

Ekaterina M. Kasianenko[1*], Anastasia V. Golovchenko[2], Vladimir I. Siplivyi[2], Oleg G. Romanov[3,4], and Olga I. Baum[1]

[1] Institute of Photon Technologies, Federal Scientific Research Center "Crystallography and Photonics", Russian Academy of Sciences, 2 Pionerskaya str., Troitsk, Moscow 108840, Russia

[2] Department of Ophthalmology, I. M. Sechenov First Moscow State Medical University (Sechenov University), 8 Trubetskaya str., Moscow 119991, Russia

[3] Belarusian State University, 4 Nezavisimosti pr., Minsk 220030, Belarus

[4] B. I. Stepanov Institute of Physics, National Academy of Sciences of Belarus, 68 Nezavisimosti pr., Minsk 220072, Belarus

*** e-mail:** ekkassianenko@gmail.com

Abstract. In many clinical cases, knowledge of the biomechanical properties of the cornea will allow for early diagnosis and also contribute to the success of treatment. The methods existing in the clinic characterize the biomechanical properties of the cornea as a whole, but do not give an idea of its local properties. One of the promising approaches to measure local changes in biomechanics is optical coherence elastography (OCE) based on phase-sensitive optical coherence tomography (OCT). In this work, the OCE method, based on the registration of small tissue deformations under an applied load, showed that the appearance and propagation of mechanical waves due to laser exposure depend on the loading of the studied biological tissue due to its tension with the application of various intraocular pressures (IOP). An analysis of inter-frame differential OCT images showed that the width of the laser impact zone on the tissue increases with increasing of IOP. An analysis of the strain amplitudes depending on the IOP at a given point revealed a correlation with the IOP value and made it possible to fix the fluidity threshold for the sample under consideration in the given experimental geometry. © 2022 Journal of Biomedical Photonics & Engineering.

Keywords: intraocular pressure; phase-sensitive optical coherent elastography; cornea; keratoconus; biomechanics.

Paper #3488 received 16 Mar 2022; revised manuscript received 27 Apr 2022; accepted for publication 02 May 2022; published online 20 May 2022. doi: 10.18287/JBPE22.08.020305.

1 Introduction

The study of the biomechanics of the cornea is of undoubted interest, since there are a number of clinical situations in which an intravital assessment of mechanical properties can help both in diagnosis and in treatment. One of the most common complications of keratorefractive surgery is iatrogenic keratoconus associated with a weakening of the strength properties of the cornea. The currently available methods for the timely detection of this pathology are imperfect, since they make it possible to make a diagnosis only in the presence of late structural deformations of the cornea. Timely detection of a decrease in the strength of the cornea would make it possible to diagnose the problem at an earlier stage and significantly reduce the risk of iatrogenic pathology. In addition, with a decrease in the strength of the cornea, there is a problem with the accuracy of determining intraocular pressure. At present, the interest in the study of the biomechanics of the trabecular apparatus is quite high. The results of the study of the mechanical strength and biochemical composition of the isolated samples of trabecular tissue show an increase in the rigidity of this structure with glaucoma. In

addition, they directly correlate with the degree of intraocular fluid outflow, and, consequently, with changes in intraocular pressures (IOP) levels. The main disadvantage of such direct measurements on samples is the very high dependence of the mechanical properties of tissues on a huge number of poorly controlled factors, such as sample hydration, careful sample preparation, patient age, individual variability, and localization of the initial sample location in the eye. As a result, the resulting data have a large scatter and can only be used to a limited extent with various theoretical constructions in the clinical prediction of the behavior of a particular eye.

Now in clinical practice, devices such as Ocular Response Analyzer (Reichert, Ophthalmic Instruments, USA) [1–7] and Corvis-ST (OCULUS, Optikgerate GmbH, Wetzlar, Germany) have found application [8–11]. Both devices (and their analogues) use a calibrated air flow to deform the cornea in the central region, and then analyze the movement of the cornea under its influence. The main purpose of these devices is to accurately measure the IOP, taking into account the individual characteristics of the cornea of a particular patient. However, in addition to their main purpose, they provide an opportunity to assess the biomechanical properties of the cornea. The obtained data characterize the biomechanical properties of the cornea generally but do not give an idea of its local properties, which can be useful in the preclinical diagnosis of keratoconus and in refractive surgery. Alternative methods for studying the biomechanics of the eye, such as Brillouin scattering [12, 13], ultrasonic elastography [14, 15], atomic force microscopy [16, 17] provide the opportunity to study local biomechanical properties but have their limitations and are currently not available to use in the clinic. One of the promising approaches that allows one measuring local changes in biomechanics is optical coherent elastography based on phase-sensitive optical coherence tomography [16–23]. OCT technology of visualization of eye structures is used to diagnose keratoconus and to monitor its treatment [24] and damaged ocular surface [25] and other eye diseases. Using this method, it is possible to identify the initial stages of diseases that are not available with a slit lamp analysis. Thus, over the years, OCT has established itself as a standard and reliable method for the analysis of eye tissue. Moreover, the OCE method is being actively developed, which makes it possible to build “maps” of tissue elasticity. The high resolution of the OCE method in terms of analysis time allows visualizing the dynamics of deformations in the eye tissues at millisecond pulses of laser exposure [22]. The high sensitivity of the method to microscopic shifts makes it possible to register tissue deformations invisible to the naked eye as a result of short-term laser exposure [26, 27], which provides information on local biomechanical properties in this zone [20–22].

The present study was carried out in order to investigate the possibilities of phase-sensitive optical coherent elastography to register laser-induced microdeformations of the cornea under various mechanical stresses.

2 Materials and Methods

The study was conducted on 4 enucleated eyes of laboratory rabbits of the chinchilla-gray breed. The study plan was approved by the local ethics committee. All procedures followed the principles set out in the 1975 Declaration of Helsinki and its 2000 revision.

Four hours after enucleation, the eyes were fixed in a laboratory setup, see Fig. 1. The pressure inside the eye was maintained using a system of communicating vessels – a needle with a diameter of 0.45 mm was inserted through the cornea into the anterior chamber of the eye, connected to a bulb of sodium chloride solution fixed on a vertical stand at a certain level. The movement of the bulb along this vertical stand made it possible to change the IOP and maintain it unchanged during the laser exposure. Evaluation of IOP was carried out by the Schiotz impression tonometer. The values were recorded in mm Hg.

Laser irradiation of the tissue was carried out with an Erbium fiber laser with a wavelength of 1.56 μm. The irradiation power was chosen to be minimal so as not to cause damage to the tissue. The pulse duration is 100 ms. To study the propagation of the deformation pattern we used an OCT elastography unit, previously used to study eye tissues [22–24], and created at the Institute of Applied Physics, Russian Academy of Sciences, Nizhny Novgorod, by a group led by V. Yu. Zaitsev, with an imaging area of 4 mm wide and 2 mm deep, the setup made it possible to obtain the dependence of internal strains on time at a rate of 80 kHz for spectral bands and 20 Hz for B-scans. The study of the cornea was carried out in the central zone along the axis of the pupil.

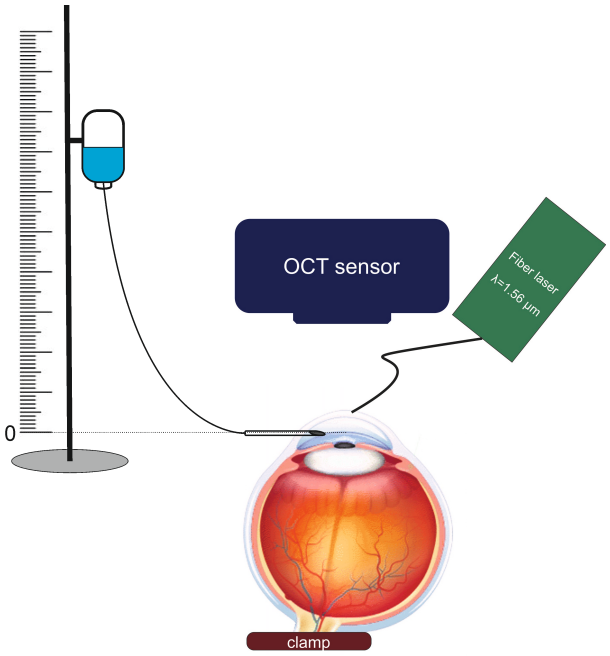


Fig. 1 The experimental setup for the study of laser-induced microdeformations of the cornea with different IOP by the optical coherent elastography.

Since the scanning frequency did not coincide with the frequency of laser pulses, from the recorded series of scans, the maxima of the width of the zone were selected, in which optocoherent elastography detected a phase change, which means that the tissue responded to laser exposure – tissue displacement and elastic wave propagation.

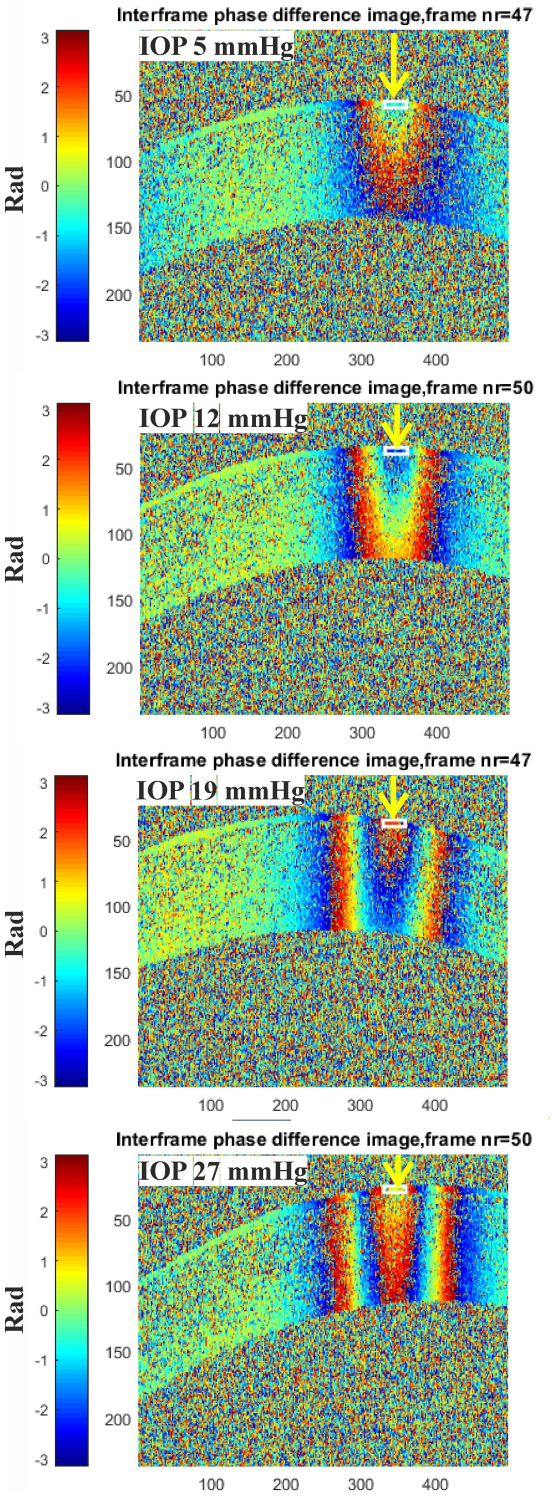


Fig. 2 Inter-frame phase difference between a pair of B-scans at the initial moment of the first laser exposure for different IOP values of the rabbit eye.

The relationship between IOP at the time of the study (and hence the mechanical stress of the cornea) and the characteristic region of elastic wave propagation under laser exposure was estimate using the Pearson parametric correlation coefficient.

Statistical analysis was performed using R version 4.1.1 (R Foundation for Statistical Computing).

3 Results

For experimental samples, no visible changes in the cornea were found in any case at the site of laser heating.

Fig. 2 shows the cornea of the eye in a depth section, along the axes the coordinates of the position in space in pixels are plotted. The axis of laser exposure is marked with a yellow arrow. The inter-frame phase difference between two consecutive B-scans exhibiting multiple phase wrapping is shown. Analysis of inter-frame differential OCT images showed that the width of the laser impact zone (area of different color – phase wrapping area) on the tissue depends on IOP (Fig. 2). Fig. 2 shows the first frame for the first laser pulse with a duration of 100 μs at different IOP of the eye (frame number 47 or 50 depending on start of recording).

Obviously, at low values of IOP, the effect of laser exposure is limited to a small area, both along the depth of the tissue and perpendicular to the axis of action. However, with an increase in IOP, the area of tissue response to laser exposure also increases.

Since the scanning frequency did not coincide with the frequency of laser pulses, frames were selected from the recorded series of scans corresponding to the maximum of the zone of phase change in the tissue, which, in fact, corresponds to the area of tissue displacement under the action of laser exposure. The characteristic size of the region of phase change was taken at half the height of the cornea with a decrease in the phase modulus by a factor of *e*.

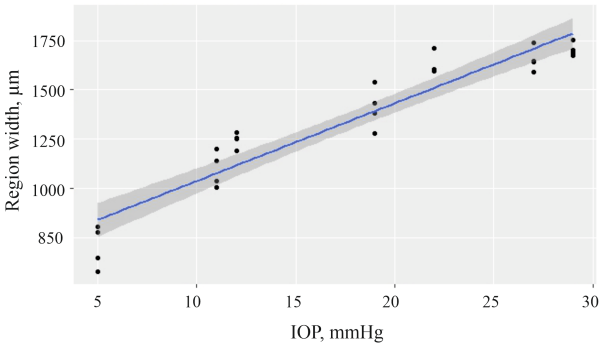
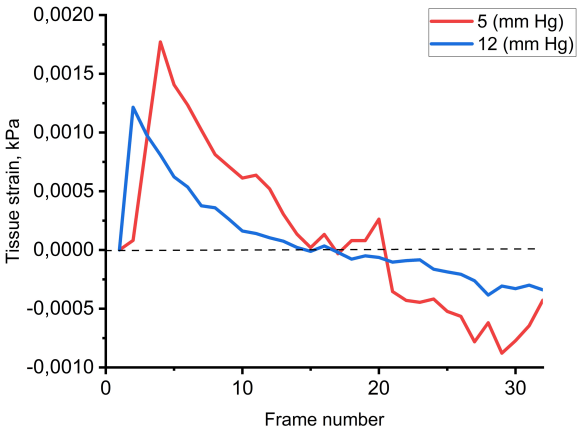
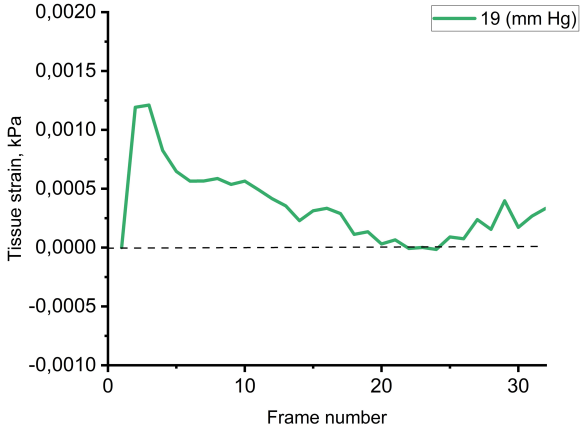


Fig. 3 Scatterplot; horizontally – IOP in mm Hg, vertically – horizontal size of the response area to laser exposure in microns.

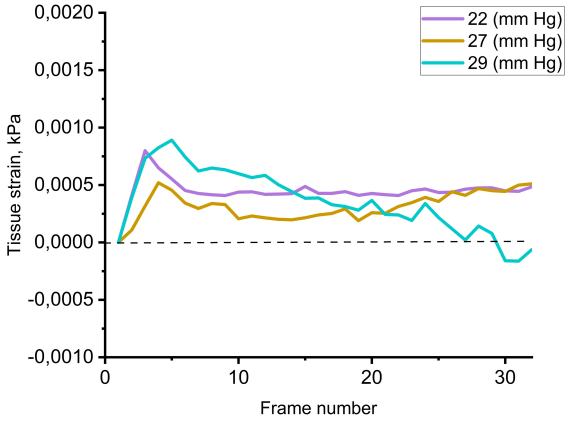
Statistical analysis showed a significant correlation between the level of IOP and the characteristic size of laser-induced microdeformation (Fig. 3). The value of the Pearson correlation coefficient was 0.94 (95% confidence interval from 0.88 to 0.97), $p < 5\times10^{-14}$.



(a)



(b)



(c)

Fig. 4 Graphs of the dependence of the amplitude of tissue strain under laser exposure of the same power on different values of IOP: (a) for IOP 5, 12 mm Hg, (b) for IOP 19mm Hg, (c) for IOP more than 20 mm Hg.

The range of propagation of the elastic wave front from the axis of laser action also differed over time for different values of IOP. So, for low IOP values, the wave propagation under laser exposure had a small depth, while at an increased IOP, the region had a significantly larger area. The wave decay rate at low IOP was higher than for high IOP.

An analysis of the amplitudes of deformations at a selected point at an equal distance from the center of laser exposure revealed the following regularities (Fig. 4): since low-power laser exposure was used in the work, which did not lead to a change or damage of the tissue structure, for a normal IOP value (19 mm Hg) deformation during laser exposure did not accumulate and relaxed completely. For low IOP, the amplitude of deformities is higher than for normal and high IOP. However, there is a rapid relaxation and reversal of the strain sign, which occurs because the tissue is not under pressure and therefore subject to oscillation. With an increase in IOP, the amplitude of deformities decreases, but the duration of their existence in the tissue becomes longer. With an increase in IOP up to 29 mm Hg laser exposure in the selected range of parameters leads to tissue fluidity, which is expressed in an increase in the amplitude of deformation and a change in their sign during relaxation.

4 Discussion

Current clinical measurements of IOP are based on indirect methods with limited accuracy because the biomechanics of the eye cannot yet be taken into account for every patient. Available systems used to measure IOP *in vivo*, such as Goldmann tonometry, Ocular Response Analyzer, dynamic contour tonometry, and non-contact tonometry, can be improved by calibration methods that take into account the mechanical properties of the cornea.

Almost all currently existing methods for assessing the biomechanical properties of biological tissues require the presence of some kind of mechanical effect on it, followed by an assessment of the deformation response. Thus, the Ocular Response Analyzer, Corvis-ST devices and their analogues used today in the clinic register the response of the cornea to a calibrated air flow acting on a sufficiently large area, which does not allow assessing the local properties of the tissue. The combination of the precise mechanical action of laser tissue heating and the sensitive technique of recording induced microdeformations using phase-sensitive coherent elastography can provide data on the local biomechanical properties of the cornea and map the biomechanical properties of the corneal tissue.

A significant reliable correlation between IOP and the recorded characteristic size of the response zone to laser-induced exposure shows the fundamental possibility of recording the mechanical stress of the cornea in a small neighborhood around the heating zone.

The development of the methodology for mapping the cornea and the improvement of methods for measuring the dynamics of the biomechanical parameters of eye tissues can be used as the basis for a method for diagnosing and monitoring the treatment of glaucoma, taking into account the biomechanical properties of eye tissues, as well as identifying a safety criterion for laser-controlled changes in the biomechanics of eye tissues. And the high resolution of the OCE method in terms of analysis time allows visualizing the dynamics of changes in the response zone in the tissues of the eye under millisecond laser pulses,

which can be a good basis for a control system of laser modification methods and treatment of eye pathologies.

5 Conclusions

Light is a non-destructive and information-intensive tool for studying biological tissues; the penetrating power of light is of particular relevance in the development of monitoring systems. Since an inherent property of light is the ability to repeatedly scatter, interacting with the components of biological tissues, the construction of clear images from the depth of the tissue is related with certain difficulties associated with the noise interference of multiply scattered radiation. To reduce noise and enhance the useful signal, methods are being developed based on the use of light coherence, as in the OCE method used in this study.

In this work, the OCE method, based on the registration of small tissue deformations under an applied load, showed that the appearance and propagation of mechanical waves due to laser exposure depend on the loading of the biological tissue due to its tension with the application of various IOPs. An analysis of inter-frame differential OCT images showed that the width of the laser impact zone on the tissue increases with increasing of IOP. An analysis of the strain amplitudes depending on the IOP at a given point revealed a correlation with the IOP value and made it possible to fix the fluidity threshold for the sample under consideration in the given experimental geometry.

In the future, the combination of the precision mechanical action of laser tissue heating and the registration of induced microdeformation using phase-sensitive coherent elastography can provide data on the local biomechanical properties of the cornea and more accurate data on the state of the IOP system of the eye, taking into account the individual characteristics of each patient.

Disclosures

All authors declare that there is no conflict of interests in this paper.

Acknowledgments

This work was supported by the Ministry of Science and Higher Education of Russian Federation within the State assignment FSRC “Crystallography and Photonics” RAS in part “Laser-induced control of pore formation depth due to additional pressures” and by an international grant by Russian Foundation for Basic Research (RFBR) (Project No. 20-52-00041 Bel a) and by the Belarusian Republican Foundation for Fundamental Research (project F20R-071) in part of “Dynamics of biomechanical properties of the cornea and sclera under laser exposure, taking into account intraocular pressure”.

References

1. G. V. Voronin, I. A. Bubnova, “Changes in biomechanical properties of the cornea after keratorefractive surgery,” Vestnik Oftalmologii 135(4), 108–112 (2019) [in Russian].
2. X. Qin, M. Yu, H. Zhang, X. Chen, and L. Li, “The mechanical interpretation of ocular response analyzer parameters,” BioMed Research International 2019, 5701236 (2019).
3. S. Koh, R. Inoue, R. Ambrósio Jr., N. Maeda, A. Miki, and K. Nishida, “Correlation between corneal biomechanical indices and the severity of keratoconus,” Cornea 39(2), 215–221 (2020).
4. M. E. Can, H. Kızıltoprak, A. D. Buluş, D. Özkoyuncu, M. Koç, and Z. Ö. Yıldız, “Corneal Biomechanical Properties in Childhood Obesity,” Journal of Pediatric Ophthalmology & Strabismus 57(2), 103–107 (2020).
5. I. A. Bubnova, S. V. Asatryan, “Biomechanical properties of the cornea and tonometry measurements,” Vestnik Oftalmologii 135(4), 27–32 (2019) [in Russian].
6. S. E. Avetisov, I. A. Novikov, I. A. Bubnova, A. A. Antonov, and V. I. Siplivyi, “Determination of corneal elasticity coefficient using the ORA database,” Journal of Refractive Surgery 26(7), 520–524 (2010).
7. M. O. Akdemir, B. T. Acar, and S. Acar, “Biomechanics in DALK: Big bubble vs manual lamellar dissection,” Arquivos Brasileiros de Oftalmologia 83(2), 87–91(2020).
8. M. Zhang, F. Zhang, Y. Li, Y. Song, and Z. Wang, “Early diagnosis of keratoconus in chinese myopic eyes by combining Corvis ST with Pentacam,” Current Eye Research 45(2), 118–123 (2020).
9. S. Shiga, T. Kojima,T. Nishida, T. Nakamura, and K. Ichikawa, “Evaluation of CorvisST biomechanical parameters and anterior segment optical coherence tomography for diagnosing forme fruste keratoconus,” Acta Ophthalmologica 99(6), 644–651 (2021).
10. S. Ren, L. Xu, Q. Fan, Y. Gu, and K. Yang, “Accuracy of new Corvis ST parameters for detecting subclinical and clinical keratoconus eyes in a Chinese population,” Scientific Reports 11(1), 4962 (2021).
11. Y. Li, Z. Xu, Q. Liu, Y. Wang, K. Lin, J. Xia, S. Chen, and L. Hu, “Relationship between corneal biomechanical parameters and corneal sublayer thickness measured by Corvis ST and UHR-OCT in keratoconus and normal eyes,” Eye and Vision 8(1), 2 (2021).
12. P. Shao, A. M. Eltony, T. G. Seiler, B. Tavakol, R. Pineda, T. Koller, T. Seiler, and S.-H. Yun, “Spatially-resolved Brillouin spectroscopy reveals biomechanical abnormalities in mild to advanced keratoconus in vivo,” Scientific Reports 9(1), 7467 (2019).

13. T. G. Seiler, P. Shao, A. Eltony, T. Seiler, and S.-H. Yun, "Brillouin spectroscopy of normal and keratoconus corneas," American Journal of Ophthalmology 202, 118–125 (2019).
14. X. Qian, T. Ma, C.-C. Shih, M. Heur, J. Zhang, K. K. Shung, R. Varma, and M. S. Humayun, "Ultrasonic microelastography to assess biomechanical properties of the cornea," IEEE Transactions on Biomedical Engineering 66(3), 647–655 (2018).
15. E. Pavlatos, H. Chen, K. Clayson, X. Pan, and J. Liu, "Imaging corneal biomechanical responses to ocular pulse using high-frequency ultrasound," IEEE Transactions on Medical Imaging 37(2), 663–670 (2017).
16. K. S. Avetisov, N. A. Bakhchieva, S. E.Avetisov, I. A. Novikov, N. V. Belikov, and I. V. Khaydukova, "Biomechanical aspects of anterior capsulotomy in cataract surgery," Vestnik Oftalmologii 133(3), 82–88 (2017) [in Russian].
17. M. R. Ford, V. S. DeStefano, I. Seven, and W. J. Dupps Jr., "In vivo measurements of normal, keratoconic, and post crosslinked keratoconic human cornea with optical coherence elastography (Conference Presentation)," SPIE Proceedings 10880, 108800X (2019).
18. M. S. Hepburn, K. Y. Foo, P. Wijesinghe, P. R. T. Munro, L. Chin, and B. F. Kennedy, "Speckle-dependent accuracy in phase-sensitive optical coherence tomography," Optics Express 29(11), 16950–16968 (2021).
19. X. Qian, R. Li, Y. Li, G. Lu, Y. He, M. S. Humayun, Z. Chen, and Q. Zhou, "In vivo evaluation of posterior eye elasticity using shaker-based optical coherence elastography," Experimental Biology and Medicine 245(4), 282–288 (2020).
20. O. I. Baum, V. Y. Zaitsev, A. V. Yuzhakov, A. P. Sviridov, M. L. Novikova, A. L. Matveyev, L. A. Matveev, A. A. Sovetsky, and E. N. Sobol, "Interplay of temperature, thermal-stresses and strains in laser-assisted modification of collagenous tissues: Speckle-contrast and OCT-based studies," Journal of Biophotonics 13(1), e201900199 (2020).
21. V. Y. Zaitsev, L. A. Matveev, A. A. Sovetsky, and A. L. Matveyev, "Quantitative Mapping of Strains and Young Modulus Based on Phase-Sensitive OCT," Optical Coherence Tomography and Its Non-Medical Applications 3, 165 (2020).
22. V. Y. Zaitsev, A. L. Matveyev, L. A. Matveev, G. V. Gelikonov, A. I. Omelchenko, O. I. Baum, S. E. Avetisov, A. V. Bolshunov, V. I. Siplivy, D. V. Shabanov, A. Vitkin, and E. N. Sobol, "Optical coherence elastography for strain dynamics measurements in laser correction of cornea shape," Journal of Biophotonics 10(11), 1450–1463 (2017).
23. F. Zvietcovich, A. Nair, M. Singh, S. R. Aglyamov, M. D. Twa, and K. V. Larin, "Dynamic optical coherence elastography of the anterior eye: Understanding the biomechanics of the limbus," Investigative Ophthalmology & Visual Science 61(13), 7 (2020).
24. A. Gokul, H. R. Vellara, and D. V. Patel, "Advanced anterior segment imaging in keratoconus: a review," Clinical & Experimental Ophthalmology 46(2), 122–132 (2018).
25. B. J. Thomas, A. Galor, A. A. Nanji, F. E. Sayyad, J. Wang, S. R. Dubovy, M. G. Joag, and C. L. Karp, "Ultra high-resolution anterior segment optical coherence tomography in the diagnosis and management of ocular surface squamous neoplasia," The Ocular Surface 12(1), 46–58 (2014).
26. O. I. Baum, G. I. Zheltov, A. I. Omelchenko, G. S. Romanov, O. G. Romanov, and E. N. Sobol, "Thermomechanical effect of pulse-periodic laser radiation on cartilaginous and eye tissues," Laser Physics 23(8), 085602 (2013).
27. O. I. Baum, A. V. Yuzhakov, A. V. Bolshunov, V. I. Siplivyi, O. V. Khomchik, G. I. Zheltov, and E. N. Sobol, "New laser technologies in ophthalmology for normalisation of intraocular pressure and correction of refraction," Quantum Electronics 47(9), 860 (2017).

Investigation of Porous Silicon Nanocomposites with Hydroxyapatite Powder Solubility

Andrey N. Agafonov[1], Diana R. Suyundukova[1*], Natalya V. Latukhina[1], and Alexander V. Pavlikov[2]

[1] Samara National Research University, 34 Moskovskoe shosse, Samara 443086, Russian Federation
[2] Moscow State University, GSP-1 Leninskiye Gory, Moscow 119991, Russian Federation

*** e-mail:** mukhametova-1993@mail.ru

Abstract. In this work, precipitation of suspensions and colloidal solutions of hydroxyapatite (HAP), porous silicon (por-Si) and por-Si+HAP nanocomposites were studied by scanning electron microscopy and Raman spectroscopy. The precipitation was carried out from suspensions with different time exposure. The noticeable solubility of the nanocomposite powder in water is shown. © 2022 Journal of Biomedical Photonics & Engineering.

Keywords: nanocomposite; hydroxyapatite; porous silicon; colloidal solution scanning electron microscope; Raman spectroscopy.

Paper #3492 received 2 May 2022; revised manuscript received 23 Jun 2022; accepted for publication 23 Jun 2022; published online 30 Jun 2022. doi: 10.18287/JBPE22.08.020306.

1 Introduction

Porous silicon (por-Si) nanocomposite with hydroxyapatite (HAP) is a promising basis of biomaterial for osteoplasty. HAP is a mineral phase of bone tissue, and ceramics based on HAP are widely used for the manufacture of bone and dental prostheses [1, 2]. In the treatment of bone tissue damage as a result of trauma or osteoporosis, to deliver HAP to the affected areas of bone, it is necessary to use transport porous particles saturated with substance, since pure HAP is practically insoluble in blood and plasma. The basis of such material can be por-Si, because of depending on the porosity, the por-Si can be both bioresistant and bioresorbable. The presence of a large number of nanoscale pores makes it possible to use por-Si as an effective matrix for creating nanocomposites, including those with hydroxyapatite [3–6]. The specific surface area, pore diameter and pore size distribution, as well as the nature and size distribution of porous particles, are important for performing the function of carrier matrices by geometric parameters regulated by synthesis conditions. The composition and condition of functional groups on the por-Si surface will depend on the anodizing conditions (current density, electrolyte composition, etc.), as well as on the choice of the brand of monocrystalline silicon [7, 8]. The current applications of por-Si for the transport of proteins, enzymes, drugs, etc. are shown [9–12]. In Ref. [6] por-Si is considered as a substrate for bone tissue growth, in Refs. [2, 7, 10, 11] por-Si nanoparticles are proposed as transport for drug delivery, in Ref. [5] por-Si is used in prosthetics technology. However, the por-Si-hydroxyappatite system as the basis of a transport nanoparticle for use in osteoplasty is not enough covered in the scientific and technical literature. The most probable reason is the problem of solubility of the por-Si + HAP nanocomposite in physiological fluids. The good solubility of por-Si is due to its high reactivity due to the large free surface area. When filling the pores of the HAP, this surface will decrease, and the HAP does not dissolve in blood and plasma. Therefore, the issue of solubility of por-Si + HAP nanocomposite in water is relevant. It was previously shown that small por-Si pores are well filled with HAP nanoparticles, which are retained in them when por-Si is ground into powder [12, 13]. With satisfactory solubility, such particles can serve as transport for the delivery of HAP to the affected areas of the bone.

The aim of this paper is to study the change in the structure of the aqueous suspension of the por-Si + HAP nanocomposite powder over time to assess the possibility of its dissolution in physiological fluids.

2 Experimental Methods

2.1 Methods of Creating Samples

To obtain por-Si samples, the method of horizontal electrochemical etching was performed. Etching was carried out in water-alcohol solutions of hydrofluoric

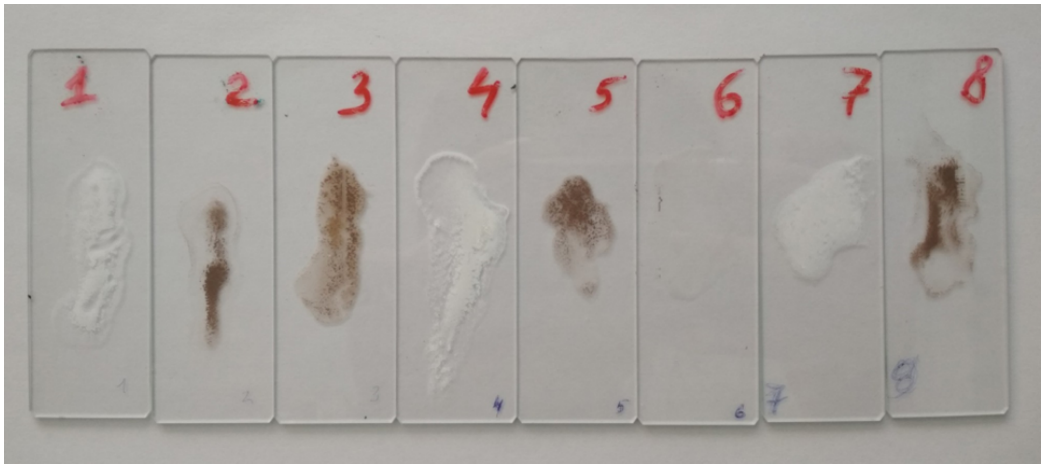


Fig. 1 The samples for the study: No. 1 HAP sediment from an aqueous suspension on the first day; No. 2 Por-Si + HAP sediment from aqueous suspension on the first day; No. 3 Por-Si sediment from aqueous suspension on the first day; No. 4 HAP sediment from aqueous suspension after a week; No. 5 Por-Si+HAP sediment from aqueous suspension after a week; No. 6 Por-Si sediment from aqueous suspension after a week; No. 7 HAP sediment from aqueous suspension in a month; No. 8 precipitation of Por-Si + HAP from aqueous.

acid for 20–30 min at an anode current density of 10 mA/cm^2. To create nanocomposites, hydroxyapatite powder (HAP) was used, which was obtained by precipitation of the bone mineral component from a demineralizing solution [14]. The HAP is deposited on a substrate from a suspension of HAP powder in ethyl alcohol or water. The deposition time was 30 min until the sample was completely dry. Por-Si and nanocomposite powders were made by mechanically separating the porous layer from the substrate and grinding it in a mortar. Based on the powders, aqueous suspensions (colloidal aqueous solutions) of por-Si, HAP, por-Si + HAP and its precipitation samples were made.

2.2 Methods of the Nanoparticles Dissolution Processes Investigation

Solubility was tested after 1 day, 1 week, and 4 weeks. At the end of the time, the suspension of each sample was planted on a slide until completely dry.

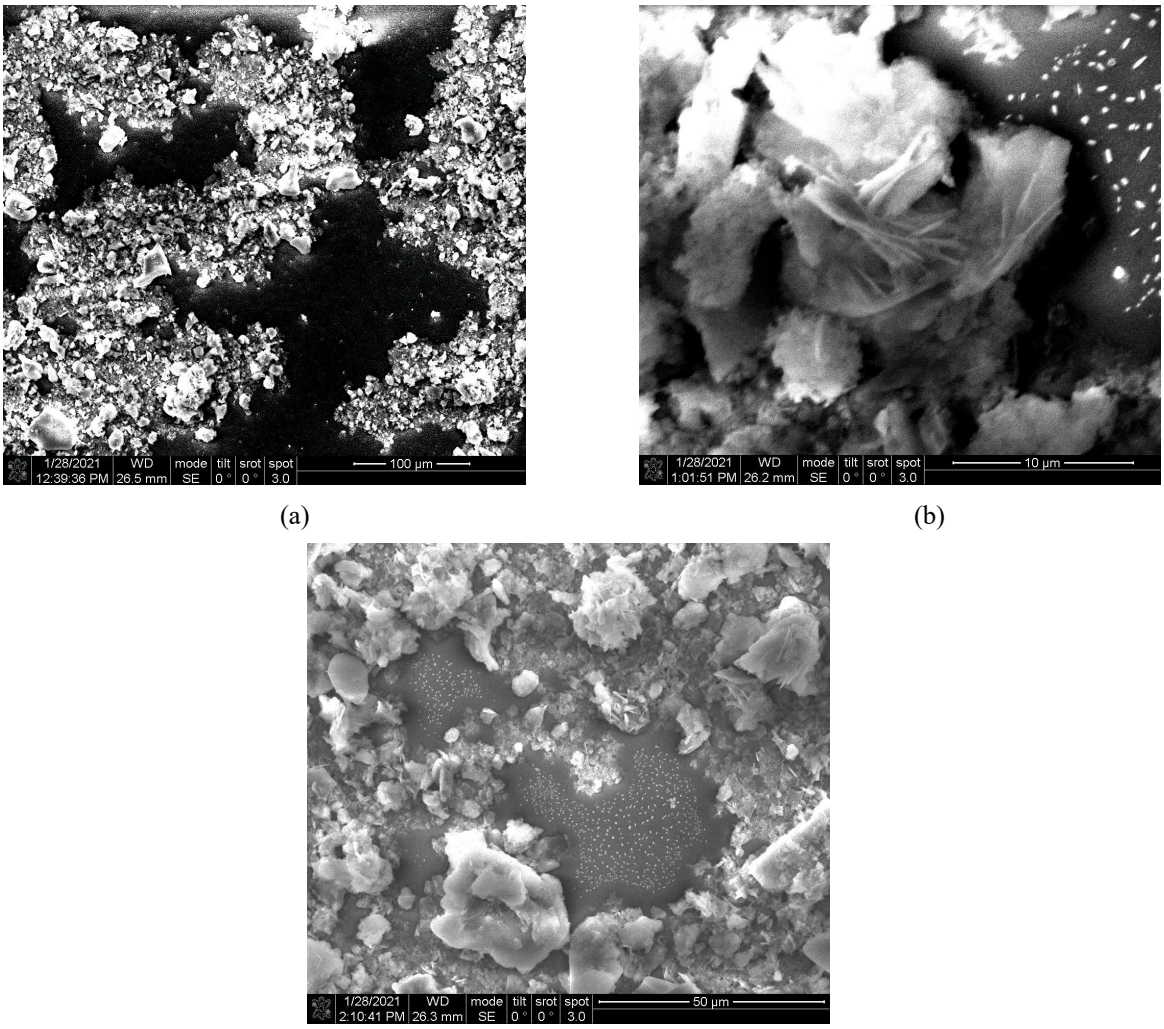
The obtained precipitation samples were studied by scanning electron microscopy (SEM) on a FEI QUANTA 200 microscope and Raman spectroscopy on a Horiba Jobin Yvon LabRam HR-800 spectrometer with a spectral resolution of 2 cm^{-1} in the 400–500 nm region, and about 1 cm^{-1} in the 500–600 nm; signal registration was carried out by a cooled CCD matrix. The excitation was carried out by an Ar+ laser at a wavelength of 488 nm.

3 Results

Fig. 1 shows glasses with the studied precipitation of suspensions. Here we can see that the precipitate of pure HAP has not been changed qualitatively either in a week or a month (No. 1, 4, 7), the precipitate of pure por-Si has become completely transparent after a week (No. 3 and No. 6), and the nanocomposite por-Si + HAP only has become slightly more transparent (No. 2, 5, 8). More precisely, an area of a more transparent solution appeared, while at the same time a darker and opaque part was preserved. This indicates that sufficiently large particles are present in the nanocomposite solution even after a month of exposure, while in the pure por-Si solution, they are practically absent after a week of exposure. This result is confirmed by the analysis of precipitation images obtained with a scanning electron microscope. Figs. 2–6 show SEM images of sediment samples from suspensions with different exposure times and their Raman spectra.

Table 1 Sample description.

Sample #	Type of sediment	Exposure time
s1	HAP from an aqueous suspension	1 day
s2	Por-Si + HAP from an aqueous suspension	1 day
s3	Por-Si from an aqueous suspension	1 day
s4	HAP from an aqueous suspension	1 week
s5	Por-Si + HAP from an aqueous suspension	1 week
s6	Por-Si from an aqueous suspension	1 week
s7	HAP from an aqueous suspension	1 month
s8	Por-Si + HAP from an aqueous suspension	1 month



(a) (b)

(c)

Fig. 2 SEM images of HAP suspension precipitation on the day of its manufacture (a, b) and after a week of exposure (c). Ruler size a) 100 µm, b) 10 µm, c) 50 µm.

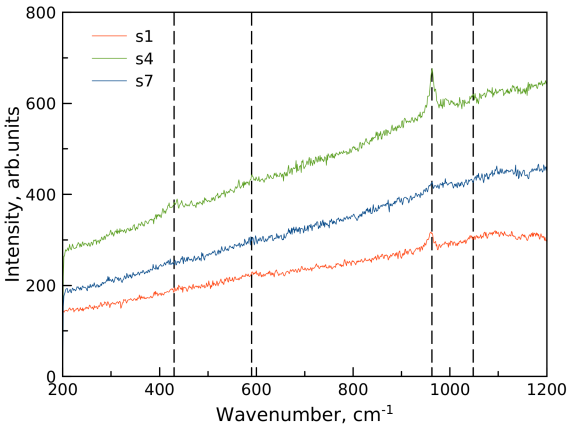


Fig. 3 Raman spectra of HAP suspensions precipitation with different exposure times: on the day of the preparation (s1), after a week (s4), and a month of exposure (s7).

Fig. 1 (a–c) shows the precipitate of the HAP suspension on the day of its preparation (a, b) and after a week of exposure (c). It can be seen that the precipitate contains two different fractions: agglomerates of large irregularly shaped particles and clusters of evenly distributed smaller particles, which have approximately the same size (0.3–0.4 µm) and a more regular form. In some agglomerates, the structure of bone tissue (b) is visible because of the natural origin of the HAP powder from the bone demineralizing solution. In the sediment from the suspension after a week of exposure (b), the agglomerates look looser, which indicates their gradual dissociation. At the same time, the average size of small particles in clusters does not change noticeably.

Fig. 3 shows the Raman spectra of samples s1, s4, s7. Vertical dotted lines indicate the position of the Raman lines in the HAP spectrum from the Ref. [15]. The analysis of the Raman spectra (Fig. 3) shows that there is no peak corresponding to the HAP in the HAP sediment spectrum of the suspension with a monthly exposure (sample s7). This may also indicate the gradual destruction of HAP agglomerates.

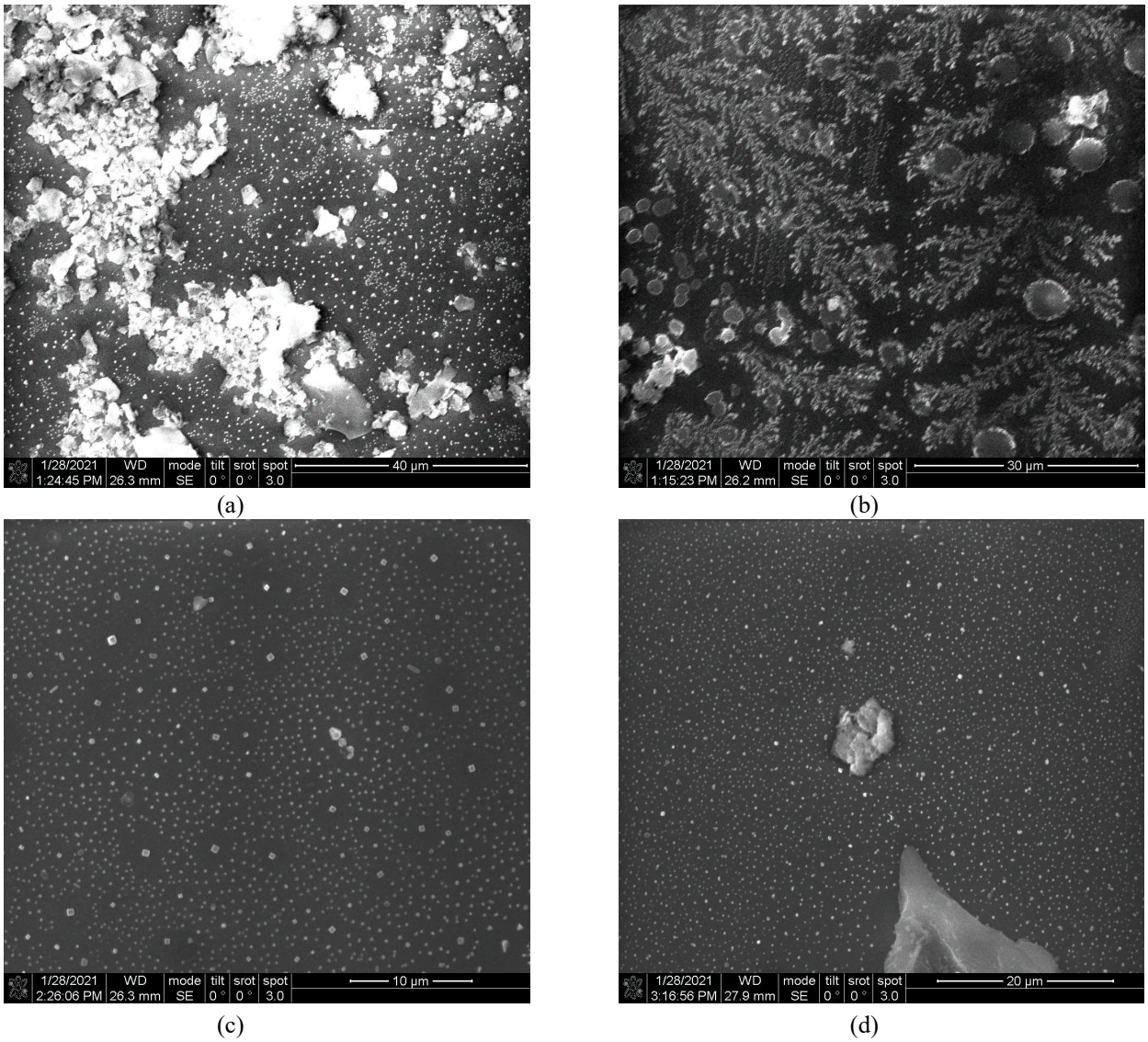


Fig. 4 SEM images of PC + HAP suspension sediments (a, b, e, f); (a, b) suspension sediment on the day of the preparation; c) after a week of exposure; d) after a month of exposure. Ruler size a) 40 µm, b) 30 µm, c) 10 µm, d) 20 µm.

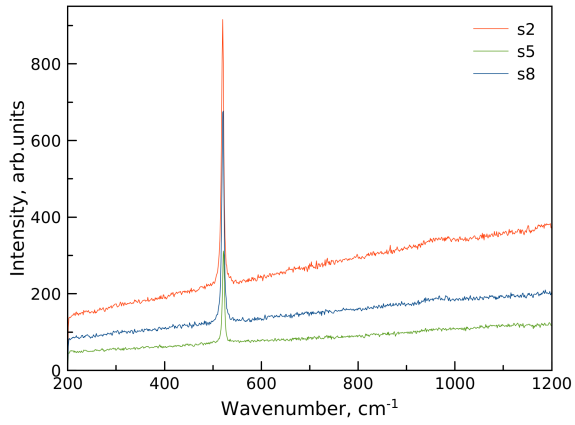
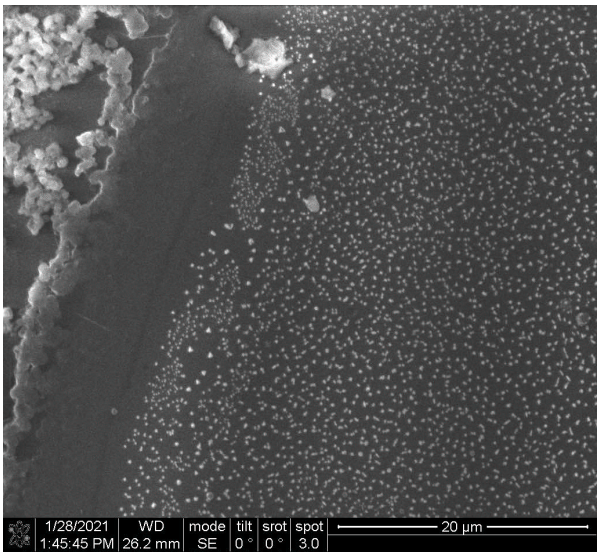


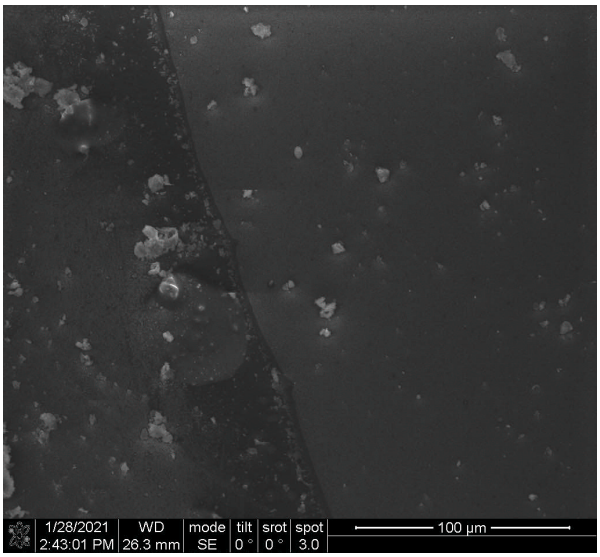
Fig. 5 Raman spectra of por-Si+ HAP suspension precipitation on the preparation day of (s2), after weekly (s5) and monthly exposure (s8).

Fig. 4 (a–d) shows the SEM images of the por-Si + HAP suspension precipitation on the preparation day (a, b), after a week (c) and a month (d) exposure. Here it is also possible to distinguish fractions of agglomerates of large, tens of micrometers, particles and clusters of uniformly distributed smaller ones with characteristic sizes of less than 1 µm. Among the small ones there are particles of regular square shape, which can be identified as silicon nanocrystals crystallizing in a cubic syngony (Fig. 4d). In addition, there is a phase of polycrystalline HAP in the form of characteristic "herringbone". Its formation indicates that very small HAP particles are present in the suspension. When the sediment dries, they crystallize into needle-like nanocrystals, which are then "folded into a herringbone" into a supracrystalline structure in the hexagonal syngony characteristic of the $Ca_{10}(PO_4)_6(OH)_2$ compound (for example, see Ref. [18]). These particles are released from nanoscale pores by grinding a porous layer saturated with HAP. A similar pattern is observed on the transverse

cleavage of a porous layer saturated with HAP from an aqueous solution after evaporation of the liquid from the pores. (Fig. 4b) [13]. Over the time, agglomerates of large particles gradually break down in the suspension (Fig. 4c, d). The number of small silicon particles also decreases, as evidenced by a noticeable decrease in the intensity of the peaks of the corresponding to silicon with a wave number of 520 cm^{-1} (Fig. 5).



(a)



(b)

Fig. 6 SEM images of por-Si suspension precipitation on the preparation day (a) and after a week (b) exposure. Ruler size a) 20 µm, b) 100 µm.

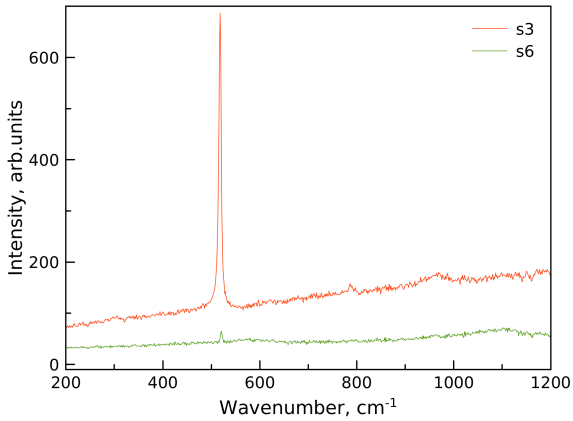


Fig. 7 Raman spectra of por-Si suspension precipitation on the preparation day (s3) and after a week of exposure (s6).

The same pattern of reduction in the number of silicon particles is demonstrated by samples of precipitation of pure por-Si suspensions both in the SEM images of Fig. 6 (a, b) and in the Raman spectra (Fig. 7), which is consistent with the data on the high solubility of porous silicon [16, 17].

4 Conclusion

The study shows that the powder of the por-Si + HAP nanocomposite is soluble in water, although to a lesser extent than the powder of the initial porous silicon without hydroxyapatite. This means that the particles of the por-Si + HAP nanocomposite can be used for HAP transport in biological fluids. Over the time, they dissolve in water, releasing nanoscale HAP particles in the pores. Therefore, we can conclude that porous silicon is a promising material for creating a biomaterial for bone implants and drugs for the treatment of osteoporosis on the basis thereof. The direction of further research should include determining the dissolution rate of the nanocomposite powder, its dependence on the size of nanoparticles in order to determine the optimal sizes of nanoparticles and the conditions for their manufacture.

Disclosures

All authors declare that there is no conflict of interests in this paper.

References

1. S. M. Barinov, V. S. Komlev, Biokeramika na osnove fosfatov kal'ciya, Nauka, Moscow (2005). ISBN 5-02-033724-2 [in Russian].

2. J. Salonen, A. M. Kaukonen, J. Hirvonen, and V. P. Lehto, "Mesoporous silicon in drug delivery applications," Journal of Pharmaceutical Sciences 97(2), 632–653 (2008).
3. C. Rey, C. Combes, C. Drouet, H. Sfihi, and A. Barroug, "Physico-chemical properties of nanocrystalline apatites: Implications for biominerals and biomaterials," Material Science and Engineering 27(2), 198–205 (2007).
4. O. I. Ksenofontova, A. V. Vasin, V. V. Egorov, A. V. Bobyl', F. Y. Soldatenkov, E. I. Terukov, V. P. Ulin, N. V. Ulin, and O. I. Kiselev, "Porous silicon and its application in biology and medicine," Zhurnal Tekhnicheskoj Fiziki 84(1) 67–78 (2014) [in Russian].
5. D. Fan, G. R. Akkaraju, E. F. Couch, L. T. Canham, and J. L. Coffer, "The role of nanostructured mesoporous silicon in discriminating in vitro calcification for electrospun composite tissue engineering scaffolds," Nanoscale 3, 354–361 (2011).
6. L. Pramatarova, E. Pecheva, D. Dimova-Malinovska, R. Pramatarova, U. Bismayer, T. Petrov, and N. Minkovski, "Porous silicon as a substrate for hydroxyapatite growth," Vacuum 76, 135–138 (2004).
7. E. Tasciotti, X. Liu, R. Bhavane, K. Plant, A. D. Leonard, B. K. Price, M. M.-C. Cheng, P. Decuzzi, J. M. Tour, F. Robertson, and M. Ferrari, "Mesoporous Silicon Particles as a Multistage Delivery System for Imaging and Therapeutic Applications," Nature Nanotechnology 3(3), 151–157 (2008).
8. V. V. Tregulov, Poristyj kremnij: tekhnologiya, svojstva, primenenie, Ryazanskiy Gosudarstvennyj Universitet named after S. A. Esenina, Ryazan' (2011). ISBN 978-5-88006-677-3 [in Russian].
9. P. G. Travkin, N. V. Voroncova, S. A. Vysockij, A. S. Len'shin, Y. M. Spivak, and V. A. Moshnikov, "Issledovanie zakonomernostej formirovaniya struktury poristogo kremniya pri mnogostadijnyh rezhimah elektrohimicheskogo travleniya," Proceedings of Saint Petersburg Electrotechnical University 4, 3–9 (2011) [in Russian].
10. V. Ya. Shevchenko, O. I. Kiselev, V. N. Sokolov et al., Issledovanie, tekhnologiya i ispol'zovanie nanoporistyh nositelej lekarstv v medicine, Himizdat, Saint-Peterburg (2015). ISBN 978-5-93808-255-7 [in Russian].
11. Yu. A. Polkovnikova, A. S. Len'shin, P. V. Seredin, and D. A. Minakov, "Porous silicon nanoparticles containing neurotropic drugs," Inorganic Materials 53, 477–483 (2017).
12. D. R. Suyundukova, N. V. Latuhina, K. A. Ganichkina, and P. V. Kazakevich, "Porous silicon and nanocomposites based on it as biomaterials," Proceedings of IV Interdisciplinary Scientific Forum with International Participation "New materials and advanced technologies" 2, 186–187 (2018) [in Russian].
13. V. Pukhova, V. Kolesnikovich, Y. Spivak, N. Latukhina, and D. Suyundukova, "Features of the Localization of HAP in Porous Silicon with Various Surface Treatments," Proceedings of the 2020 IEEE Conference of Russian Young Researchers in Electrical and Electronic Engineering, 1000–1003 (2020).
14. E. V. Pisareva, V. G. Podkovkin, E. A. Yulaev, and E. N. Arkhipova, "Features of the dynamics of demineralization of human and rat bone tissue in morphological studies," Vestnik Samarskogo Gosudarstvennogo Universiteta 7(47), 167–171 (2006) [in Russian].
15. E. Timchenko, E. V. Timchenko, E. V. Pisareva, M. Yu. Vlasov, L. T. Volova, O. O. Frolov, and A. R. Kalimullina, "Experimental studies of hydroxyapatite by Raman spectroscopy," Journal of Optical Technology 85(3), 130–135 (2018).
16. A. F. Alykova, I. N. Zavestovskaya, V. G. Yakunin, and V. Y. Timoshenko, "Raman diagnostics of silicon nanocrystals dissolution in aqueous medium," Journal of Physics: Conference Series 945, 012002 (2018).
17. A. F. Alykova, "Optical Methods for Diagnostics of Silicon Nanoparticles for Application in Biomedicine," Sbornik trudov XVI Vserossijskogo Molodezhnogo Samarskogo Konkursa – Konferencii Nauchnyh Rabot po Optike i Lazernoj Fizike, Moskva, 41–49 (2018). ISBN 978-5-902622-39-0 [in Russian].
18. Bioactive glass, Mo-Sci Corporation (accessed 1 May 2022) [https://mo-sci.com/products/bioactive-glass/].